COMPUTER VISION AND MACHINE LEARNING METHODS FOR THE ANALYSIS OF BRAIN AND CARDIAC IMAGERY

A Thesis
Presented to
The Academic Faculty

by

Vandana Mohan

In Partial Fulfillment
of the Requirements for the Degree
Doctor of Philosophy in the
School of Electrical and Computer Engineering

Georgia Institute of Technology
May 2011

COMPUTER VISION AND MACHINE LEARNING METHODS FOR THE ANALYSIS OF BRAIN AND CARDIAC IMAGERY

Approved by:

Professor Jeff Shamma, Committee Chair
School of Electrical and Computer Engineering
Georgia Institute of Technology

Professor Allen Tannenbaum, Advisor
School of Electrical and Computer Engineering
Georgia Institute of Technology

Professor Anthony Yezzi
School of Electrical and Computer Engineering
Georgia Institute of Technology

Professor Scott Wills
School of Electrical and Computer Engineering
Georgia Institute of Technology

Professor Oskar Skrinjar
School of Biomedical Engineering
Georgia Institute of Technology

Date Approved: October 29, 2010

To my parents for always standing by me and my dreams,

and to thatha *for teaching me never to settle or give up.*

ACKNOWLEDGEMENTS

I want to thank my adviser Dr. Allen Tannenbaum for being a great teacher of not just computer vision, but also of life. Your ever-positive and down-to-earth spirit and your constant curiosity and passion for learning have been even more of an influence on me than your obvious brilliance! I would also like to thank John Melonakos, Ganesh Sundaramoorthi and Marc Niethammer for their contributions to the technical and mathematical side of this research, and Nathalie Agar, Marek Kubicki and Arthur Stillman for being the most amazing clinical collaborators, and making this research endeavor the constant learning journey that I have so tremendously enjoyed. A special thanks to Nathalie for your high energy and enthusiasm! Not only have I learned a great amount about cancer and mass spectrometry from you, your infectious optimism and goodness of spirit are qualities that I hope to emulate! I would also like to thank all my fellow students from Minerva - Yi Gao, Xavier LeFaucheur, Delphine Nain, Yan Yang, Shawn Lankton, Jimi Malcolm, Gallagher Pryor, Rome Sandhu, Ivan Kolesov, Jacob Huang, Peter Karasev, Liang-Jia Zhu and Jehoon Lee. You have all been the source of much education, encouragement and inspiration! A special thanks to Steve Marzec for linux installations, MATLAB help and more! Thanks also to Gerardo Hermosillo Valadez and Yoshihisa Shinagawa for being the most amazing mentors at Siemens Medical Solutions and teaching me so much about breast cancer and more, it was definitely one of the busiest and best summers!

Now for my family in Atlanta... Rahul Ghosh, Nisha Rajagopalan, Himani Jain, Nandita Yeshala, Sucharita Shankar, Prashant Warier, Anu and Farzan and Baby Bharucha, Anupama Kasturirangan, Deepak and Asha Jahagirdar, Nisarga Naik, Murtaza Motiwala, Valas Valancius. This far from home, you have made me realize time and again why friends are the family we choose for ourselves. Thank you for all the crazy adventures and your

kindness and presence when I needed it. You have turned Atlanta into a second home for me and for that I will always love you all.

Most of all I want to thank my parents Seshachari and Padma Mohan, who have always stood by me and my dreams, and my brother Srinivasan Mohan, sister-in-law Ranjini Venkat and friend for life Krithika Srinivasan for their unconditional love and support. You keep me grounded while giving me the strength to dream. I couldn't have done this without you. Thank you for loving me for who I was, am and will be :)

TABLE OF CONTENTS

LIST OF TABLES

LIST OF FIGURES

SUMMARY

Medical imagery is increasingly evolving towards higher resolution and throughput. The increasing volume of data and the usage of multiple and often novel imaging modalities necessitates the use of mathematical and computational techniques for quicker, more accurate and more robust analysis of medical imagery. The fields of computer vision and machine learning provide a rich set of techniques that are useful in medical image analysis, in tasks ranging from segmentation to classification and population analysis, notably by integrating the *qualitative* knowledge of experts in anatomy and the pathologies of various disorders and making it applicable to the analysis of medical imagery going forward. The object of the proposed research is exactly to explore various computer vision and machine learning methods with a view to the improved analysis of multiple modalities of brain and cardiac imagery, towards enabling the clinical goals of studying schizophrenia, brain tumors (meningiomas and gliomas in particular) and cardiovascular disorders.

In the first project, a framework is proposed for the segmentation of tubular, branched anatomical structures, notably neural fiber bundles and blood vessels. A tubular shape model is proposed and the corresponding analytical techniques derived for its application in segmentation. Also, a novel branch detection algorithm is proposed for the automatic detection of branches in the structure being segmented, and the proposed framework is successfully applied to the segmentation of neural fiber bundles and blood vessels.

In the second project, a population analysis framework is built using the shape model proposed as part of the first project. This framework is successfully applied to the analysis of neural fiber bundles towards the detection and understanding of schizophrenia. Alternate co-registration techniques are explored for the neural fiber bundles, and a detailed discussion of the applicability and generalization of the results is presented.

In the third and final project, the use of mass spectrometry imaging for the analysis of brain tumors is motivated on two fronts - towards the offline classification analysis of the data, and the end application of intraoperative detection of tumor boundaries. SVMs are applied for the classification of gliomas into one of four categories towards application in building appropriate treatment plans, and multiple statistical measures are studied with a view to feature extraction (or biomarker detection). The problem of intraoperative tumor boundary detection is formulated as a detection of local minima of the spatial map of tumor cell concentration which in turn is modeled as a function of the mass spectra, via regression techniques.

0.1 Roadmap

In Chapter 1, we introduce the fields of computer vision and medical imaging that this thesis falls under and discuss the specific research problems that are addressed in the scope of this thesis. We briefly discuss the challenges in these areas and then summarize the contributions of this thesis.

In Chapter 2, we present a detailed discussion of the first research problem i.e., the segmentation of tubular anatomical structures. The motivation, a discussion on prior work in this area, as well as the mathematical and implementation details of the proposed segmentation framework are presented in this chapter along with the corresponding results for the applications of neural fiber bundle and cardiac vessel segmentation.

In Chapter 3, the details of the population study framework (based on the tubular surface model from Chapter 2) are presented. The mathematical framework is presented and the results and findings from the population study are presented with a discussion of the same.

In Chapter 4, the work in the area of Mass Spectrometry Imaging analysis is discussed. First, the classification framework for MSI analysis is presented and the use of statistical measures for biomarker detection is motivated, along with a discussion of the results obtained. Next, the proposed framework for tumor boundary detection is presented, with a detailed discussion of the mathematics for the RVM-based regression, the results, and a short preview of the problems to be addressed in future work towards establishing a complete intraoperative tumor boundary detection framework.

Finally, in Chapter 5, we conclude with some remarks for future research directions on each of these fronts.

CHAPTER I

INTRODUCTION

In this chapter, the fields of computer vision and machine learning are introduced with specific focus on the analysis of medical imagery of the brain and cardiac regions, and the contributions of this thesis are summarized.

1.1 Overview

Computer vision is a subset of the field of Artificial Intelligence. It aims to imitate human vision via computers towards the goal of automatic decision making in such varying fields as industrial automation, medical image analysis and military tracking [39]. Machine learning is a related field of research which is aimed at analysing large amounts of data towards extracting complex patterns from the same. Both these fields of research find great application in the analysis of medical imagery, since with the advances in medical image acquisition techniques, not only have the resolution and information captured improved tremendously but also the amount and complexity of the data to be analysed has increased thereby neccessitating the development of better algorithms that can meaningfully analyse this data. In line with this, brain and cardiac image acquisition have progressed tremendously in recent years notably with the advent of Diffusion-Weighted Magnetic Resonance Imaging (DWI) for studying white matter (WM) properties in the brain and Computer Tomographic Angiography (CTA) for studying the structure of the heart and vasculature. While both these modalities yield greater resolution than previously available techniques, their usage presents new challenges by way of the large size of the imaging data sets, the insufficiency of intensity information for separating out structures of interest and the absence of adequate ground truth to train detection algorithms with. A third imaging modality that has captured tremendous interest is Mass Spectrometry Imaging. Classically used for

the analysis of the chemical composition of samples, Mass Spectrometry is gaining interest as a method of medical imaging wherein the data representing the chemical composition of a medical sample is treated as an image and methods for computer vision and machine learning are applied to the analysis of this data. This modality presents various challenges in data analysis such as the large size of the data for each sample, but most significantly the fact that the interpretation of this data as imagery is as yet being defined.

The research performed in the scope of this thesis focuses on dealing with each of these three kinds of imagery towards the goals of detection of disorders such as schizophrenia, atheroclerosis and brain tumors (particularly gliomas). We propose a novel segmentation framework for tubular anatomical structures, especially for the neural fiber bundle segmentation from brain DWI and vessel segmentation from cardiac CTA data. This leads to an elegant population analysis framework that uses this novel segmentation framework towards disorder detection and characterization in brain DWI data, and acts as a bridge between our contributions to computer vision (image segmentation) and machine learning (group studies in schizophrenia) by combining concepts from both fields. Finally, we address the analysis of Mass Spectrometric Imaging and motivate the application of machine learning techniques to the same, towards the end-goal of integrating mass spectromety imaging as an intraoperative medical imaging modality.

CHAPTER II

TUBULAR TREE SEGMENTATION FRAMEWORK

2.1 Motivation

In this chapter, we propose a novel segmentation framework, motivated initially by the problem of segmenting neural fiber bundles from Diffusion-Weighted Magnetic Resonance Imagery (DW-MRI or DWI). Neural fiber bundles are challenging to segment owing to the noisy nature of DWI data, and the absence of expert agreement or ground truth on the boundaries of these structures. We begin by observing that neural fiber bundles display a tubular geometry with relative uniformity around a center-line. We therefore propose a Tubular Surface model where each structure of interest (i.e. a neural fiber bundle) is represented as a tubular surface in 3D space, and we further develop some key relationships that allow us to achieve computational efficiency and further extend the framework into other applications such as group studies (which is discussed in greater detail in Chapter 3). Further, we observe that the tubular surface assumption is also applicable to other structures such as blood vessels and develop the required extensions to the framework for this application.

In this chapter, we present the complete methodology, the background math and derivations, the implementation details and the experiments and results obtained for the two target applications of fiber bundle segmentation from brain DWI data and blood vessel segmentation from cardiac Computer-Tomography Angiography (CTA) data. Note that this framework was inspired by prior work building the level set segmentation framework based on the Finsler tractography work of [61], to extract structures of interest from imagery in oriented domains (or vector-valued imagery). A short summary of that work is presented in Appendix B.

2.2 Anatomical structures of interest and prior work

The proposed framework can be applied to extract any tubular branched structure from either scalar or vector-valued imagery. In this work, we focus on segmenting two anatomical structures - the Cingulum Bundle (CB), which is of potential interest in the diagnosis of schizophrenia, and the human vasculature, which is of interest for studying cardiovascular disorders such as atherosclerosis. The subsequent sections discuss the physical description and anatomical significance of these structures as well as prior work in the areas of segmenting the respective structures. While it is outside the scope of this specific work to discuss other neural fiber bundles in detail, for the purpose of illustrating the framework's usability, we demonstrate that the proposed framework also applies successfully to the external and internal capsules. For further information about these and other neural fiber bundles, interested readers are referred to [78].

2.2.1 The Cingulum Bundle

The Cingulum Bundle is a 5-7 mm in diameter fiber bundle that interconnects all parts of the limbic system. It originates within the white matter (WM) of the temporal pole, and runs posterior and superior into the parietal lobe, then turns, forming a "ring-like belt" around the corpus callosum, into the frontal lobe, terminating anterior and inferior to the genu of the corpus callosum in the orbital-frontal cortex [78]. It consists of long, association fibers that directly connect temporal and frontal lobes, as well as shorter fibers radiating into their own gyri.

It is a *thin, highly curved* structure that consists of a collection of neural fibers, which are mostly disjoint, possibly intersecting, roughly aligned and centered around a fiber. The collection of fibers approximately forms a tube-like structure. Because of its involvement in executive control and emotional processing, the CB has been investigated in several clinical studies, including studies of depression and schizophrenia. The CB and other fiber bundles can be imaged through a modality called diffusion weighted magnetic resonance imaging

(DW-MRI). This is an image in which each voxel consists of a collection of numbers that can be used to determine the amount of diffusion of water in various directions. A tensor at each voxel can be associated with the collection of numbers, and such an image is called a diffusion tensor magnetic resonance image (DT-MRI). Previous studies of schizophrenia using DT-MRI demonstrated decrease of FA in anterior part of the cingulum bundle [45, 90], at the same time pointing to the technical limitations restricting these investigations from following the entire fiber.

The diffusion pattern in the CB varies in orientation and anisotropy smoothly along the structure, and it has a distinct diffusion pattern from surrounding areas of the brain (see Fig. 3 for a sagittal slice of the CB). The CB is challenging to segment because of inhomogeneity of its diffusion pattern *globally* and the noisy nature of DW-MRI makes it difficult to detect edges separating the CB from the rest of the image.

There has been much research in detecting and characterizing neural connections between brain structures in DW-MRI. Early methods for detecting fibers, i.e., *tractography*, are based on streamlines where the fiber path is constructed by following the direction of the principal eigenvector of diffusion tensors from an initial seed point, e.g., [67, 19]. These methods have been shown to perform poorly in noisy situations and they often terminate prematurely before the fiber ending. To alleviate these problems, a number of works, e.g.,[74, 73, 32, 47, 1, 101, 18], construct an optimal path between a starting and ending seed. The procedure is repeated to detect all fibers of a bundle.

In this work, we segment the entire fiber bundle as a volumetric region enclosed by a surface. It is typically difficult to segment the CB using standard active surface techniques, e.g. [98, 99], adapted to DW-MRI, since the DW-MRI of the brain is extremely noisy and contains many local features that could trap the active surface in unlikely configurations. Standard region-based techniques adapted to DW-MRI or DT-MRI, e.g. [46], are generally not applicable to the segmentation of the CB since the statistics of the DW-MRI inside the CB cannot be described by a few *global* parameters (e.g. mean). The Mumford-Shah

energy extended to DT-MRI, [92], which assumes piecewise smooth image data inside the surface, is applicable to the CB. However, the assumption of smoothness outside the surface is not valid because of many different structures outside the brain with varying diffusion patterns. In [4], the authors perform segmentation of the CB by treating the problem as a voxel classification problem. An energy is formulated that is maximum when the estimated probability distributions of the classes are maximally separated (in the sense of entropy). The method, as the Mumford-Shah approach, assumes two distribution classes one for the foreground (the CB) and one for the background, which is multi-modal and hence not well described by a Gaussian distribution as done in the work. Noticing that standard region-based techniques are not applicable to the CB, an edge-based active surface method for segmenting the CB is considered by [62]. However, the method is sensitive to the noise in the DW-MRI. The work of Melonakos et al [63] designs an energy on volumetric regions that incorporates "local region-based" information and a prior favoring regions that are close to an initially detected center-line curve. However, the energy is highly dependent on the correct placement of the detected center-line, which is often not exactly in the center of the CB. The work in [29] follows a template-based approach by aligning a deformable fiber-bundle model to the subject tensor field, which has significant improvements over tracking individual fibers.

2.2.2 Blood Vessels in Cardiac Imagery

Blood vessel extraction from imagery is vital to surgical planning and the diagnosis of cardio-vascular disorders such as atherosclerosis. There are several techniques based on deformable models for vessel extraction; however, they have limitations that we attempt to address in this work. In [56], the authors evolve a three dimensional (3D) curve to align it to the boundary of vessels determined by image edges; the method only provides a single curve in the vessel not the entire volumetric region. In [88], a flux-maximizing flow on curves/surfaces is constructed to align the curve/surface normal along the gradient direction

of the image. To take into account the geometrical shape of a vessel, the authors of [68] construct a geometric shape prior to favor vessel-like structures and combine it with image region statistics to deform the curve/surface to capture the vessel. In [60], a method based on image histogram information is used to deform an initial vessel tree that was obtained by registration of the image to a pre-segmented reference image. The methods [88, 68, 60] do not explicitly model the tubular nature of the vessel(s) to be detected. Therefore in [50], the authors model vessels as the envelope of a collection of spheres, thus having a explicit tube-like model for the vessel. The segmentation is performed based on a minimal path technique [17]. The centerline is detected without any additional effort in comparison to methods which process the segmentation to obtain a centerline (e.g. [10]). The drawback of the method of [50] is that it requires that the user inputs the endpoints of the vessel branch. There has also been work on modeling vessels as a combination of a center-line and a chosen cross-sectional shape ([8, 71, 52]). In [31], the center-line is modeled as a 1-D B-spline curve and a 3D surface evolution approach is employed to fit the vessel wall along the curve. Similarly, [66] uses a 3D active surface to model the vessel branch, with axial constraints applied, and [87] puts forth a level set-based approach with an initial centerline. [48] provides an excellent review of lumen segmentation methods which combine models of vessel appearance and geometry with image features.

Amongst the reviewed methods, we note the methods that are related to the proposed method in their use of intensity information and/or incorporation of shape (tubularity). These include the use of statistical distributions for modeling the intensity range of tissues of interest ([30, 2]), coupled appearance models that combine information about the intensity distributions of the tissue of interest and the background ([59, 95]), geometric models such as surface models of tubularity ([31]) and models of center-line and crosssection ([70, 52]).

The above works are of two forms: 1) vessels are represented by a general deformable surface allowing one to capture in particular tree-like vessel structures or 2) branches of

the vessel are modeled by parametric cylinder-like tubes. The former has the disadvantage of having many degrees of freedom that the approach is susceptible to undesirable local minima and is computationally costly while the latter is not flexible enough in that it cannot explicitly deal with branching of the tubular structure (specifically, the blood vessel).

2.2.3 Novelty of the Proposed Framework

In this work, we model the CB as a tubular surface and blood vessels as tubular trees. A tubular surface is represented as being completely defined by a center-line and an associated radius function at every point of the center-line (see Figure 1). Since the tubular surfaces that we consider are determined by this combination of a center-line in 3D space and a corresponding scalar radius function, the extraction problem can be reduced to optimizing an energy defined on 4D curves, which *significantly reduces the computational cost of the optimization procedure when compared to an unconstrained deformable surface*. A benefit of our approach is that the center-line is automatically obtained through the extraction process. This provides a skeleton of the vessel tree, which facilitates fly-through visualization to gauge plaque deposits and stenosis in the vessel interior. Our method was inspired by the work of [50] in which the authors model vessels as tubular regions formed by the union of spheres along a center-line. Energies are constructed on 4D curves that represent tubes, and these energies are globally minimized using the minimal path technique [17]. The energies we construct cannot be optimized using the minimal path technique since our energies are directionally dependent - they depend on the position of the 4D curve and its *tangent*. Moreover, for the energies that we consider, we are not interested in a global minimum but rather certain local minima.

The advantage of our approach over existing methods in blood vessel extraction is a model of the vessel tree that is general enough to capture entire vessel trees while having much fewer degrees of freedom than a general deformable surface alleviating susceptibility to undesirable local minima and keeping the computational cost low. We do this

by proposing a tubular tree model and a corresponding automatic branch detection and evolution method that can be initialized by as few as a single seed point. Other methods [56, 66, 31, 50] that use tube-like representations for the vessel can either deal with only a single branch or in order to capture multiple branches of the vessel tree, multiple seed points or initial regions for each individual branch must be chosen. Further, there is no guarantee that several of the tubes representing branches by the latter approach will not overlap in configurations that are unrealistic for vessel trees. Finally, while branch detection (in the blood vessel tree) has previously been addressed as a problem in itself (e.g. [102],[91]), it is dealt with as a problem that follows the complete segmentation of the surface or the skeletonization of the structure of interest.

2.3 Methodology

2.3.1 Tubular Surface Model

We model a tubular surface as being determined by a center line that is an open curve in $\mathbb{R}^3$, and a radius function defined at each point of this center-line. Given an open curve $c : [0, 1] \to \mathbb{R}^3$, the center line, and a function $r : [0, 1] \to \mathbb{R}^+$, the radius function, we can define the tubular surface, $S : \mathbb{S}^1 \times [0, 1] \to \mathbb{R}^3$ ($\mathbb{S}^1$ is $[0, 2\pi]$ with endpoints identified) as follows:

$$S(\theta, u) = c(u) + r(u)[n_1(u)\cos\theta + n_2(u)\sin\theta] \tag{1}$$

where $n_1, n_2 : [0, 1] \to \mathbb{R}^3$ are normals to the curve c defined to be orthonormal, smooth, and such that the dot products $c'(u) \cdot n_i(u)$ vanish. See Figure 1 for an illustration of a tubular surface. The tubular surface is represented as a collection of circles each lying in the plane perpendicular to the center line. Note that the surface in (1) may thus be identified with a 4D space curve, $\tilde{c} : [0, 1] \to \mathbb{R}^4$:

$$\tilde{c}(u) = (c(u), r(u))^T. \tag{2}$$

This representation of a surface as a space curve has the additional advantage of significantly reducing the computational complexity of our algorithm.

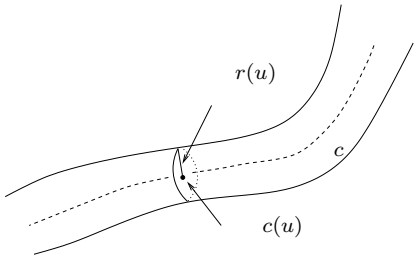

Figure 1: Illustration of proposed Tubular Surface model

2.3.2 Defining Energies for Segmentation

We now define a general class of energy functionals on the space of 4D curves - as in Equation (2) - whose optimum represents the structure of interest, i.e., the CB from brain DWI, or the blood vessel from cardiac CTA imagery. Note that while we derive the expressions with respect to the structure of DWI data (i.e, imagery in an oriented domain), the scalar CTA imagery can be thought of as a special case of imagery in an oriented domain with only one sampling direction.

Let $\mathbb{S}^2 \subset \mathbb{R}^3$ denote the unit sphere, which represents the set of all possible angular acquisition directions of the scanning device for DWI. Let $I : \mathbb{R}^3 \times S^2 \rightarrow \mathbb{R}^+$ be the diffusion image. We are interested in weighted length functionals on 4D curves as energy functionals of interest. Indeed, let $\Psi : \mathbb{R}^4 \times S^2 \rightarrow \mathbb{R}^+$ ($\Psi(x, r, v) \in \mathbb{R}^+$) be a weighting function, which we call the *potential* to be chosen, and define the energy as

$$E(\tilde{c}) = \int_{\tilde{c}} \Psi(\tilde{c}(\tilde{s}), \frac{c'(\tilde{s})}{|c'(\tilde{s})|}) \, \mathrm{d}\tilde{s}, \;\; \tilde{c} = (c, r) \tag{3}$$

where $\mathrm{d}\tilde{s} = |\tilde{c}'(u)| \, \mathrm{d}u = \sqrt{(r'(u))^2 + |c'(u)|^2} \, \mathrm{d}u$ is the arclength measure of the 4D curve, and $c'(\tilde{s})/|c'(\tilde{s})|$ is the unit tangent to c, the center line. When (3) is minimized, the term $\mathrm{d}\tilde{s}$ penalizes the non-smoothness of the center line and the radius function. The energy (3) is related to the length of a curve in a Finsler manifold [76, 75, 61].

For segmenting the CB, the goal is to choose Ψ so that the energy is optimized by a $\tilde{c}$ which determines a surface enclosing the diffusion pattern of the CB in the DW-MRI of the

brain. The diffusion pattern in the cingulum varies in orientation and anisotropy across the length of the bundle, although being *locally* similar, and that pattern differs from the pattern immediately outside the CB. This fact precludes the use of traditional region-based techniques adapted to DT-MRI since these techniques assume homogeneous statistics within the *entire* region enclosed by the surface, whereas we will assume homogeneity within local regions. The idea is to choose Ψ at a particular coordinate (x, r, p) to incorporate statistics of the DT-MRI *local* to the disc determined by (x, r, p) rather than using statistics global to the entire structure as in traditional region based methods.

Along similar lines, for vessel segmentation, the weighting function, Ψ, is chosen to maximize the difference in mean intensities inside and outside the discs centered along the center-line [65]. Notice that here again, the statistics employed are not global to the entire structure but rather local to the discs determined by (x, r, p).

In Section 2.3.4, we give examples of potentials that can be employed for the segmentation of the Cingulum Bundle and blood vessels, respectively.

2.3.3 Energy Optimization

In this section, we construct a steepest descent flow to minimize the energy of interest (3). A steepest descent is considered since we are not necessarily interested in the global maximizer or minimizer; indeed, the energy corresponding to (14) does not have a global maximizer. We begin with a tubular surface initialization i.e., an initial 4D curve, and follow the gradient (or its opposite depending on whether we want to maximize or minimize the energy under consideration).

2.3.3.1 Gradient Descent: Fixed Endpoints

The standard technique for calculating the gradient of an energy defined on curves, which is based on a geometrized $\mathbb{L}^2$ metric on the space of curves, cannot be applied to our energy of interest. This is because of the fact that when minimizing (3) using $\mathbb{L}^2$, Ψ must satisfy a certain positivity condition (see [61]) that we cannot guarantee for our choices of Ψ

otherwise the gradient descent is ill-posed. Moreover, when maximizing (3), we are indeed maximizing a weighted length, which with respect to the standard geometrized $\mathbb{L}^2$ curve metric, leads to an *unstable reverse diffusion*. As shown in [82], such weighted length functionals may be optimized in a *stable* manner by moving in the gradient direction of the energy (3) with respect to a *geometrized Sobolev metric*:

Definition Let $\tilde{c} : [0,1] \to \mathbb{R}^4$ be such that $\tilde{c}(0)$, $\tilde{c}(1)$ are fixed. Let $h, k : [0,1] \to \mathbb{R}^4$ be perturbations of $\tilde{c}$ then

$$\langle h, k \rangle_{\mathbb{L}^2} := \frac{1}{L} \int_{\tilde{c}} h(\tilde{s}) \cdot k(\tilde{s}) \, \mathrm{d}\tilde{s}, \tag{4}$$

$$\langle h, k \rangle_{\text{Sob}} := L \int_{\tilde{c}} h'(\tilde{s}) \cdot k'(\tilde{s}) \, \mathrm{d}\tilde{s}, \tag{5}$$

where L is the length of of the curve $\tilde{c}$, $\mathrm{d}\tilde{s}$ is arclength element of $\tilde{c}$, and the derivatives are with respect to the arclength parameter $\tilde{s}$.

It can be shown that the gradient of (3) with respect to the Sobolev metric above is

$$\frac{1}{L} \nabla_{\text{Sob}} E(\tilde{c}) = K(\Psi_{\tilde{p}}) + \partial_{\tilde{s}} K(\hat{\Psi}_v \sqrt{1 + (r_{\tilde{s}}/|c_{\tilde{s}}|)^2} + \Psi \tilde{c}_{\tilde{s}}), \tag{6}$$

where

$$K(f) := \int_0^L K(\cdot, \tilde{s}) f(\tilde{s}) \, \mathrm{d}\tilde{s}, \tag{7}$$

$$K(\tilde{s}_1, \tilde{s}_2) = \frac{1}{L} \begin{cases} \frac{\tilde{s}_2}{L}(1 - \frac{\tilde{s}_1}{L}) & 0 \le \tilde{s}_2 \le \tilde{s}_1 \\ \frac{\tilde{s}_1}{L}(1 - \frac{\tilde{s}_2}{L}) & \tilde{s}_1 \le \tilde{s}_2 \le L \end{cases}. \tag{8}$$

$\Psi_{\tilde{p}}$ is the partial derivative of the energy function Ψ with respect to the position p, and Ψ_v is the partial derivative with respect to orientation v (with $\hat{\Psi} v$ denoting the projection of this 4D vector down to the 3D space in which the tubular surface resides).

The detailed derivation of these expressions is given in the Appendix A.1.

This expression has the additional numerical advantage that only first order derivatives are required in comparison to the standard $\mathbb{L}^2$ gradient, which needs second order information, and which cannot be used anyway since it results in an unstable flow. Note that as stated in [82], the expression (6) may be computed efficiently in order N complexity, where N is the number of sample points of the curve.

2.3.3.2 Evolving Endpoints

In the previous subsection, we derived a gradient descent flow for (3) provided the endpoints of the 4D curve (i.e., the end cross sections of the tube) are fixed. We now describe how to evolve the endpoints so as to reduce the energy. This is useful for some choices of Ψ in (3), for example, Ψ_2 defined in (14), and more importantly in applications such as vessel segmentation where the endpoints of the structure of interest are not known *apriori*. To determine the evolution of the endpoints, we compute the variation with respect to the endpoints. This results in

$$\begin{aligned} \tilde{c}_t(0) &= \mp\hat{\Psi}_v\sqrt{1+\left(\frac{r_{\tilde{s}}}{|c_{\tilde{s}}|}\right)^2} \mp \Psi\tilde{c}_{\tilde{s}}, \\ \tilde{c}_t(1) &= \pm\hat{\Psi}_v\sqrt{1+\left(\frac{r_{\tilde{s}}}{|c_{\tilde{s}}|}\right)^2} \pm \Psi\tilde{c}_{\tilde{s}}, \end{aligned} \tag{9}$$

which will minimize/maximize the energy (depending on the sign chosen above). Therefore, the algorithm to reduce the energy is to alternatively evolve the 4D curve by (6) and the endpoints by (9).

2.3.4 Examples of Potentials for Segmentation, Ψ

In this section, we give two choices of Ψ that are meaningful for extracting the CB from brain DWI, both based on *local* region-based statistics and a usable expression for vessel segmentation which separates the local region statistics as discussed in Section 2.3.2.

The first potential Ψ_1 (for CB segmentation) at a coordinate $(x, r, v) \in \mathbb{R}^3 \times \mathbb{R}^+ \times \mathbb{S}^2$ is constructed so as to be small when the *mean diffusion profile* inside the disc, $D(x, r, v)$, differs greatly from the mean diffusion profile inside the annular region, $D(x, \alpha r, v) \backslash D(x, r, v)$

where $\alpha > 1$, outside $D(x, r, p)$. This is given by the following expressions:

$$\Psi_1(\tilde{p}, v) = \frac{1}{1 + \|\mu_{D(\tilde{p},v)} - \mu_{D((p,\alpha r),v)\setminus D(\tilde{p},v)}\|^2} \tag{10}$$

where the μ's are the means:

$$\mu_{D(\tilde{p},v)}(\hat{v}) = \frac{1}{r^2} \int_{D(\tilde{p},v)} I(x, \hat{v})\, \mathrm{d}A(x) \tag{11}$$

$$\mu_{D((p,\alpha r),v)\setminus D(\tilde{p},v)}(\hat{v}) = \frac{1}{(\alpha^2 - 1)r^2} \int_{D((p,\alpha r),v)\setminus D(\tilde{p},v)} I(x, \hat{v})\, \mathrm{d}A(x). \tag{12}$$

Here $\mathrm{d}A$ is the area element and $\|\cdot\|$ is a suitable norm on functions of the form $f : \mathbb{S}^2 \to \mathbb{R}^+$, e.g.,

$$\|f_1 - f_2\|^2 = \int_{\mathbb{S}^2} |f_1(v) - f_2(v)|^2\, \mathrm{d}S(v), \tag{13}$$

where $\mathrm{d}S$ is the surface area element. The energy corresponding to Ψ_1 is *minimized*.

The second potential is chosen such that the corresponding energy is related to a weighted surface area:

$$\Psi_2(x, r, p) = r \int_0^{2\pi} \phi(x + r p^{\perp}(\theta))\, \mathrm{d}\theta, \quad \text{and } p^{\perp}(\theta) = n_1 \cos\theta + n_2 \sin\theta \tag{14}$$

where n_1, n_2 are orthonormal vectors perpendicular to p, and $\phi : \mathbb{R}^3 \to \mathbb{R}^+$ is large near the boundary of differing diffusion regions, e.g.,

$$\phi(x) = \frac{1}{|B(x, R)|} \int_{B(x,R)} \|I(y, \cdot) - \mu_{B(x,R)}(\cdot)\|^2\, \mathrm{d}y. \tag{15}$$

Here $B(x, R)$ is the ball centered at x of chosen radius R, $|B(x, R)|$ denotes the volume, and the norm is defined as in (13). Here, we are interested in *maximizing* the corresponding energy. The objective is to initialize the tubular surface inside the CB, and increase surface area until the surface reaches the boundary of differing diffusion patterns.

For the application of blood vessel segmentation, where we aim to maximize the difference in mean intensities inside and outside the discs centered along the center-line, the energy function for vessel segmentation is given as:

$$\Psi(\tilde{p}, v) = \mu_{D(\tilde{p},v)} - \mu_{D((p,\alpha r),v)\setminus D(\tilde{p},v)}. \tag{16}$$

As above the μ's are the means:

$$\mu_{D(\tilde{p},v)}(\hat{v}) = \frac{1}{r^2}\int_{D(\tilde{p},v)} I(x)\,\mathrm{d}A(x) \tag{17}$$

$$\mu_{D((p,\alpha r),v)\setminus D(\tilde{p},v)}(\hat{v}) = \frac{1}{(\alpha^2-1)r^2}\int_{D((p,\alpha r),v)\setminus D(\tilde{p},v)} I(x)\,\mathrm{d}A(x). \tag{18}$$

In the latter expression $\mathrm{d}A$ is the area element and $I(x) \in \mathbb{R}^+$ is the image intensity at a given position x. Notice that the energy (to be maximized) uses *local* region-based statistics to separate the tube's interior and exterior in comparison to traditional region-based approaches which separate the global mean intensities inside and outside the surface (e.g. [13]). It is thus suited to vessel structures where the image intensity varies smoothly along a vessel (but is not necessarily constant). Note also the dependence of Ψ on $\hat{v}$, which is the orientation of the disk.

2.3.5 Initialization Methodology

In this work, we have adopted a variational approach for optimizing the energies used to segment the CB and blood vessels. Since the approach yields a local minimum (or maximum) the performance of the proposed framework is sensitive to the initialization, of both the center-line and the cross-sectional radius of the tubular surface. In segmenting the blood vessel tree, it is not viable to know the end points of each branch *a priori* and hence we only apply the Moving Endpoints implementation to blood vessel segmentation. In segmenting the CB, since the fiber bundle is made up of distinct fibers, the task of selecting

a center-line for initialization is analogous to the tractography problem and we can use both implementations.

In our experiments with the Fixed Endpoints implementation for fiber bundle segmentation, we use the Finsler tractography approach of [62, 76, 75, 61], which given a seed region and a target region, constructs an optimal connection on the Finsler manifold between the two regions, using an optimal measure of connectivity based on the Finsler metric. We use this method since while in data with only 6 gradient directions, the Finsler metric based approach becomes equivalent to a Riemannian metric-based approach, in the case of high angular data such as the data used in the experiments for the results included in this thesis, the Finsler metric allows more flexibility than the Riemannian metric since it does not impose an ellipsoidal diffusion profile on the data. We use the dynamic programming based approach from [76, 75, 61] which is based on the fast sweeping method, and yields optimal connectivity maps and characteristic vectors at every point of the domain. Following these characteristic vectors back from the target region to the seed region then yields the ”optimal” path connecting the two regions and we use this as the center-line (referred to as the *Anchor Tract*) to initialize the Fixed Endpoints implementation of the proposed framework. Alternate initialization methods that hold potential include streamlining-based tractography algorithms. It is worth noting that this optimal path is referred to as the “anchor tract,” terminology put forth in [76, 75, 61]. Thus, for segmenting the CB using the fixed end points implementation of the proposed algorithm, a perturbation of the anchor tract is used as the initial centerline curve and the smallest possible radius of 0.5 is used, with the surface essentially growing out from this initial radius.

For the Moving Endpoints implementation in both fiber bundle and blood vessel segmentation, initialization is carried out with the user providing a set of one or more seed points in the structure of interest, preferably close to the center-line and a guess for initial radius. (Note that this implies that the overall proposed segmentation framework is to be classified as a semi-automatic segmentation framework.)

2.3.6 Branch Detection

While we have modeled the CB as a single tubular structure, in reality, it is a tubular structure encompassing discrete neural fibers, which further has branches that are essentially connections from the CB to surrounding gray matter regions in the brain. More importantly, the vasculature displays a branching and thinning geometry as well, and in order to meaningfully segment blood vessels, it is necessary to capture an entire vessel tree. The branching nature of the structures of interest poses a challenge in applying the tubular surface segmentation framework directly, since we want to automatically detect branches in the vicinity of the evolving structure, as it grows out, and then construct new tube(s) to capture the detected vessel branches.

The proposed branch detection algorithm is summarized in Algorithm 1. Note that with the goal of improving computational efficiency, the branch detection step is performed each time an end point moves significantly (rather than at every iteration).

2.4 Experiments and Results

In this section, we present the results from the application of the proposed framework to fiber bundle and blood vessel segmentation. To illustrate the framework's utility in fiber bundle segmentation, the Cingulum Bundle was focused upon. The framework was applied to a DWI data set (of 54 subjects) that included schizophrenic and normal control subjects (27 each), with the DWI being acquired for 51 sampling directions. Results visualized here show the CB extracted for both the right and left bundles in some randomly selected cases out of this data set. The results were also compared qualitatively with the results from the neural fiber bundle segmentation framework of Melonakos et al [63, 61]. The experiments to demonstrate the use of the algorithm in blood vessel segmentation were conducted on a CTA data set that included data from healthy subjects (with no plaque) as well as subjects with varying degrees of plaque and stenosis. The framework was also tested on the Rotterdam CTA data set [77], and quantitative validation is provided.

Algorithm 1 Branch detection algorithm

Construct a sphere S^2 of radius R (a function of the input guess for typical vessel radius) centered at the end point under analysis.

Sample N directions $d_i \forall i \in (1, N)$ uniformly off this sphere S^2.

Construct tubes of radius 1 and length R along each of the N directions, originating at the end point under analysis.

Estimate the mean image intensity within each tube as $I_{mean}(d_i)$.

Threshold the estimated mean intensities with respect to the parent branch intensity I_{thres}.

Extract the subset of directions d_i off the sphere S^2 with mean intensities above the threshold.

Apply k-means clustering [41, 38] to the extracted directions $d_i \forall i \in (1, N)$ and $I_{mean}(d_i) >= I_{thres}$, with a target of 3 clusters.

if Number of non-empty clusters < 3 **then**

Declare non-existence of branching at end point under analysis

else

Compute the centroid of the directions in each cluster, to yield 3 candidate branch directions.

Eliminate the candidate direction that has maximum overlap with the parent branch's volume.

Compute the dot products of the 2 remaining candidate directions with the tangent of the parent branch at the end point.

Extend the parent branch by the candidate direction better aligned with the tangent at the end point.

Create a new branch in the tree structure using the 1 remaining candidate direction.

end if

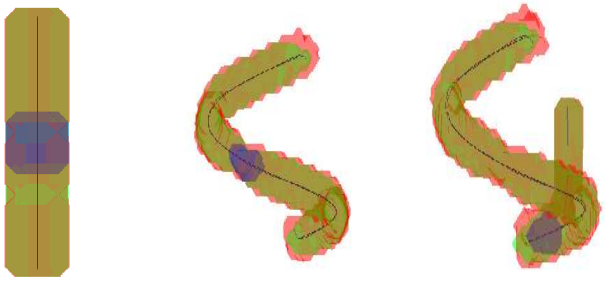

Figure 2: Results of experiments with Moving Endpoints Implementation on synthetic imagery: the target structure (green), the segmentation result (red), the extracted center-line (black), the true centerline (blue), and the initial volume (blue). The first and second image are structures without branches, and the third image is a structure with a branch that our algorithm correctly detects.

2.4.1 Synthetic Imagery

In this set of experiments, the proposed framework was applied to both scalar and vector synthetic images with various curvilinear branched structures. Both the implementations of the algorithm were tested on these synthetic images. Figure 2 shows the ground truth, segmentation results and associated center-line for the experiments with the Moving Endpoint implementation of the algorithm on the synthetic vector imagery. On average, the set-symmetric difference of the result with respect to ground truth was found to be $\sim 4\%$ across different synthetic structures of average radius 3 voxels.

2.4.2 CB Segmentation with Fixed Endpoints

The DW-MRI imagery used in this work was acquired on a 3T magnet using an echo planar imaging (EPI) DTI Tensor sequence with a double echo option to reduce eddy-current related distortions with 8 baseline scans and data acquired in 51 directions. The population comprised 54 male subjects (27 normal, 27 schizophrenic) spanning the age group of 21-55 years.

In this section, we show the results of applying the Fixed Endpoints implementation of the proposed framework to brain imagery of 2 subjects from this population. We use

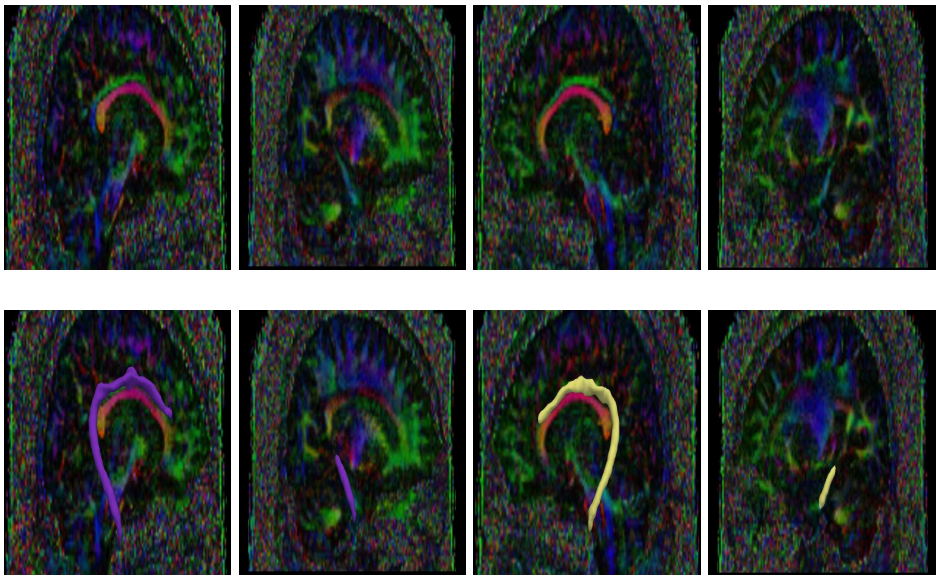

Figure 3: Selected slice-wise views of CB Segmentation results from proposed framework (with Fixed Endpoints). The top row shows the DW-MRI data and the bottom row shows the DW-MRI data with the extracted surface rendered in 3D.

the energy (3) using the potential Ψ_1 (10). Figure 3 shows slice-wise views of the CB segmentation results obtained from the proposed framework indicating the homogeneity of the discs within the captured volume. Figures 4, and 5 show the tubular surface extracted by the proposed algorithm. The surfaces shown in Figure 3 are the boundary locations rounded off to the grid points by the visualization process.

With regard to the parameter α, the ratio between the outer and inner discs of the tube, we conducted experiments using a range from 2 to 5. We observed that as this value increases, the statistics for outside the disc are averaged over a larger area thus rendering them decreasingly effective in separating intensities within the tube and just outside it. For instance, with a value of α larger than 4, we saw that the captured volume begins to leak into neighboring structures with strong diffusion such as the Corpus Callosum. From these initial experiments, we observed that a value of 3 yielded the most optimal results, with respect to balancing a capture of the maximum possible crosssectional area of the CB against leaking into the Corpus Callosum, and hence we used this in subsequent experiments.

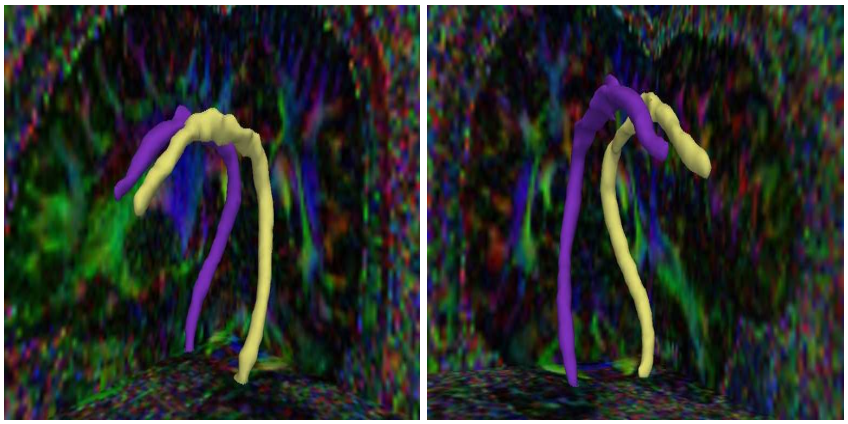

Figure 4: CB Segmentation Results (with Fixed Endpoints) for Brain data set 1: Left CB (yellow), Right CB (magenta)

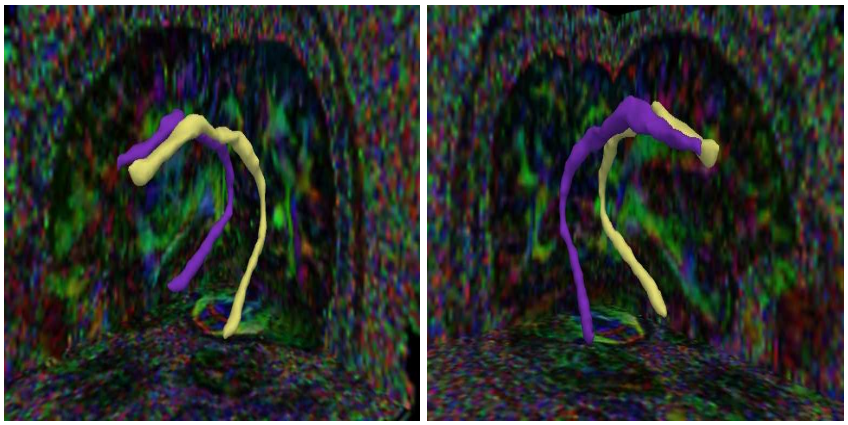

Figure 5: CB Segmentation Results (with Fixed Endpoints) for Brain data set 2: Left CB (yellow), Right CB (magenta)

2.4.3 CB Segmentation with Moving Endpoints

The Moving Endpoints implementation for CB segmentation, requires seed points in the interior of the CB near the start along with a guess for the initial radius. We applied the framework to segment the left and right Cingulum Bundle from all 20 data sets in the population under study (however, all visualizations cannot be presented in this paper). Figures 6 and 7 show the results of applying the Moving Endpoints implementation to segmenting the CB (both right and left) from brain data of two subjects (one normal and one schizophrenic).

Figure 8 shows the 3D visualization of the segmentations obtained for the Cingulum bundle and other tubular fiber bundles, i.e., the External Capsule and the Internal Capsule.

Finally, we observe that quantitative studies are not possible in neural fiber bundle analysis due to the absence of ground truth. However, we compare the results of the proposed framework with the results of the Geodesic Tractography Segmentation framework of Melonakos et al ([62, 63]). This comparison is provided in Figure 9. Note that the proposed framework outperforms [62, 63] in some key ways. Firstly, due to the lack of constraints on the end points, the proposed framework extracts the neural fiber bundle to its true length as observed by diffusion patterns rather than being limited by the approximate ROIs provided by experts. Secondly, since the method enforces the tubular geometry as it propagates outwards, it is more robust to noisy data. This is especially highlighted by the fourth case (fourth row) in Figure 9, where [62, 63] leaks into the Corpus Callosum while the proposed framework does not leak. It is also worth noting that the CB extracted by the proposed framework passes through exactly the ROIs defined by the experts, which is further validation of the accuracy of the segmentation result.

Finally, it is to be noted that the Tubular Surface model is especially advantageous for neural fiber bundle analysis since the model naturally allows sampling of features along the length of the fiber bundles, which is simultaneously useful both in performing population studies on the neural fiber bundles, as well as characterizing the discrimination ability of local regions of the fiber bundles. This is demonstrated in the context of Schizophrenia

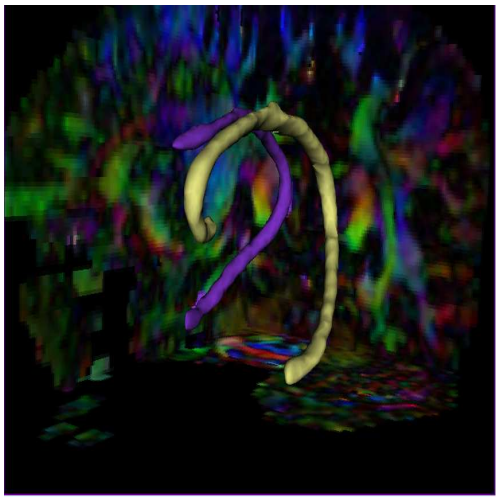

(a)

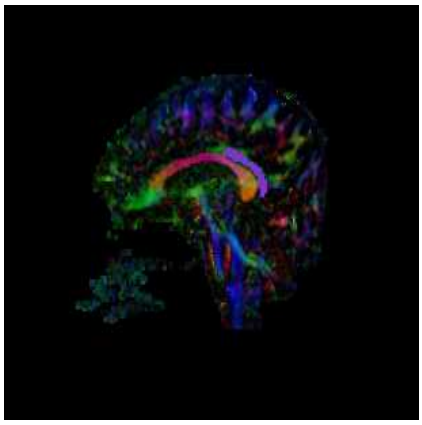

(b)

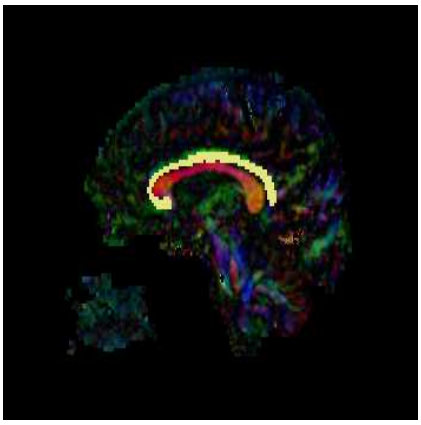

(c)

Figure 6: CB Segmentation results (with Moving Endpoints) for Brain data set 3: Left CB (yellow), Right CB (magenta). (a) shows the 3D visualization, (b),(c) show the slice-wise views.

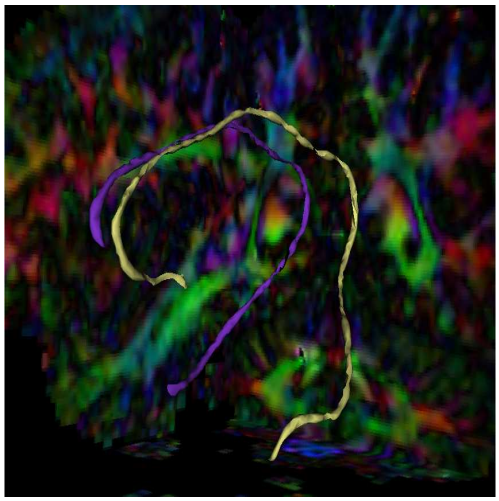

(a)

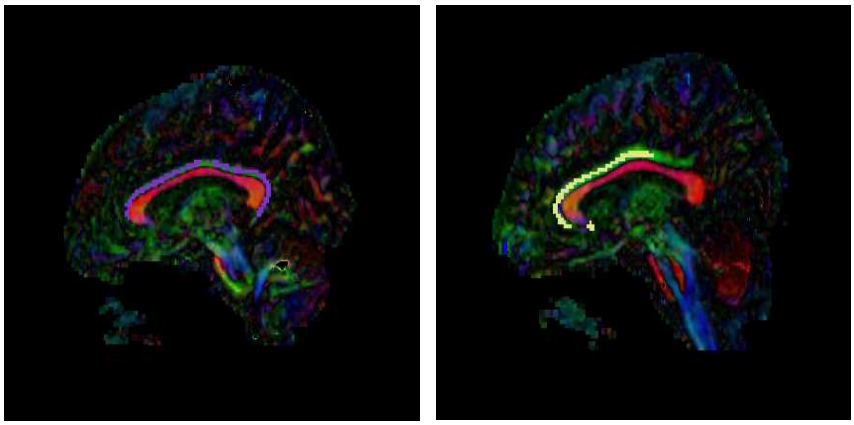

(b) (c)

Figure 7: CB Segmentation results (with Moving Endpoints) for Brain data set 4: Left CB (yellow), Right CB (magenta). (a) shows the 3D visualization, (b),(c) show the slice-wise views.

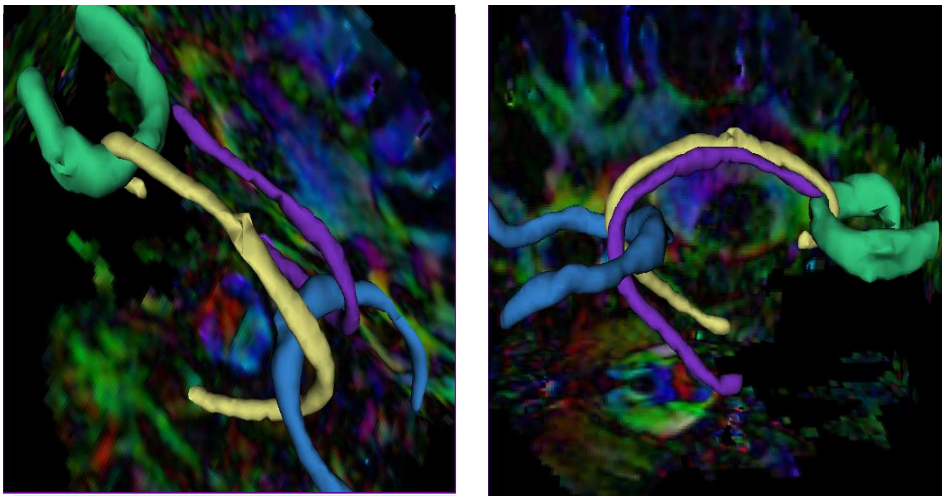

Figure 8: 3D Visualization of segmentation results showing usefulness of framework (with Moving Endpoints) for multiple fiber bundles: Left CB (Yellow), Right CB (Magenta), Internal Capsule (Green), External Capsule(Dark blue)

detection in the work of Mohan et al. [64] and the interested reader can find details on the population analysis framework therein. This population analysis framework is also described in detail in Chapter 3.

2.4.4 Blood Vessel Segmentation

We apply the Moving Endpoints implementation to vessel segmentation, because it only requires a seed point for initialization in a single branch. With regard to the parameter α, the ratio between the outer and inner disc radii, we conducted initial experiments using a range from 2 to 5. We observed that as this value increases, the statistics for outside the disc are in fact being averaged over a larger area thus rendering them decreasingly effective in separating intensities within the tube and just outside it, while a lower value rendered the functional more likely to be affected by noise. From these initial experiments, we observed that a value of 3 yielded good results and hence we have used this in subsequent experiments.

The algorithm was first tested on a population of cardiac data sets acquired from a Siemens Sensation 64 slice CTA machine. The framework was initialized with 1 user-input point at the root of the vessel tree, and a guess for typical vessel radius which guided

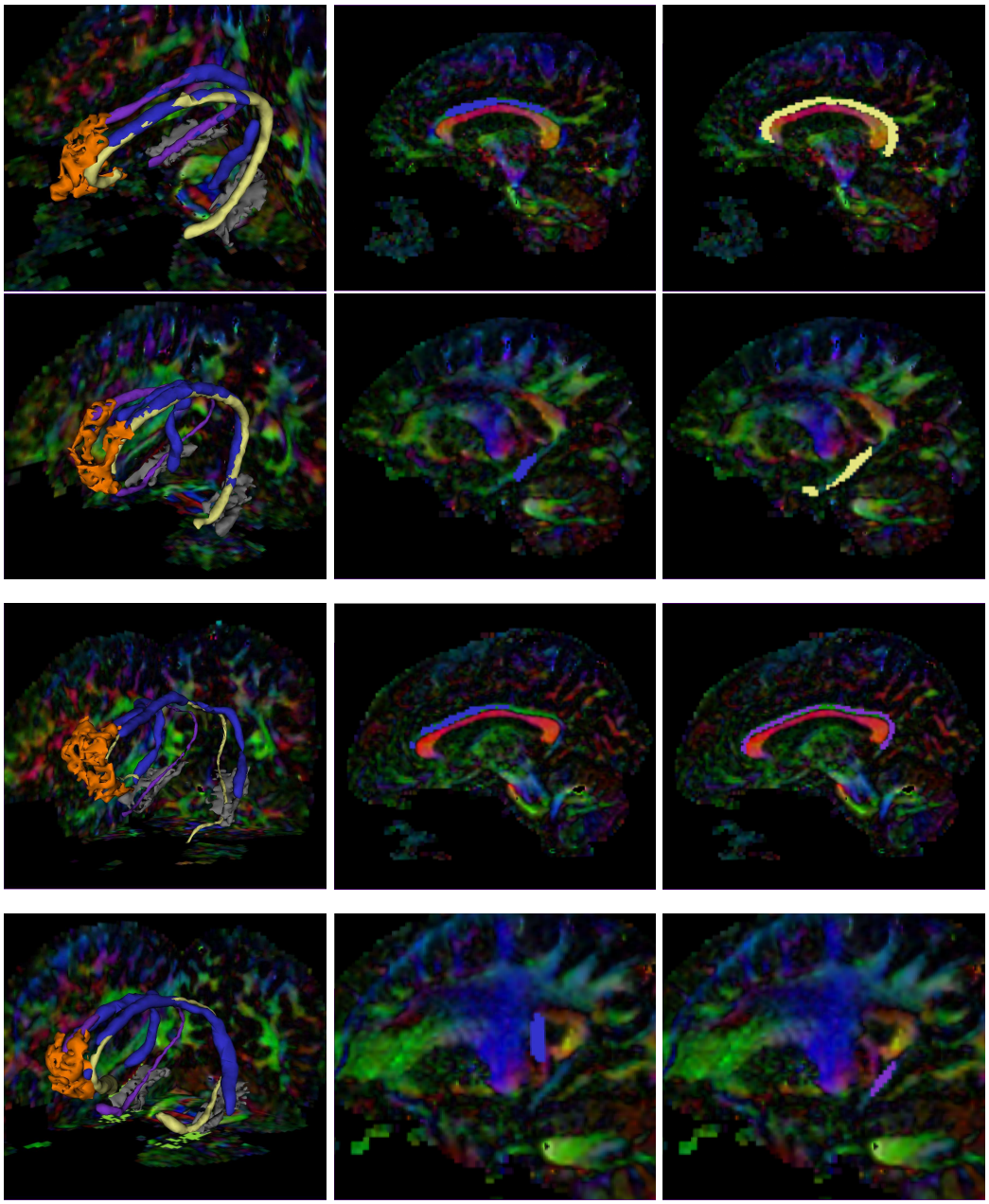

Figure 9: Visual comparison of results from proposed framework with the framework of Melonakos et al [62]: CB segmentation results from [62, 63] (blue), Left CB segmentation from proposed framework (yellow), Right CB segmentation from proposed framework (magenta), expert ROI markings for Rostral Anterior Cingulate (orange) and Parahippcampal gyrus (grey); Each row represents DW-MRI from a different subject, with the first two rows representing data from schizophrenic subjects, and the last two from normal controls. The first column shows the 3D visualization of the extracted CB for both frameworks, and the expert-marked ROIs used as input for [62]. The second column shows a slice visualization of the fiber bundle extracted (for one side) by the framework of [62] and the third column shows the same view for the proposed framework, both superimposed on the tensor data. Note that the results from [62] are limited by the input ROIs and leak into neighboring fiber bundles (note the fourth row), while the proposed framework follows the true diffusion pattern hence capturing greater lengths of the fiber bundles, and it does not leak into neighboring structures.

the branch detection process.

We first show here the results for three of the data sets tested on, for the Left Anterior Descending (LAD) coronary artery. Figures 10 and 12 show the 3D visualization of the segmented vessel trees for two cases. Also shown in these figures is the extracted centerline. The algorithm captures the branching structure automatically and successfully handles the thinning structure of the vessel tree, from the root to tips. Figures 11 and 13 show the corresponding slice-wise views of the segmentation result. We can clearly see that the framework copes well with the non-uniform contrast within the vessel volume, and is capable of following an entire vessel ~ 200 voxels in length, from the simple 1-point input used for these CTA datasets. Finally in Figure 14, we show the tubular tree evolving in 3D for a third case, illustrating how the branch detection works to capture the entire tree. These results have been qualitatively validated by medical collaborators.

We have performed quantitative validation via testing on the dataset provided as part of the Rotterdam Coronary Artery Algorithm Evaluation Framework [77]. The proposed segmentation framework was applied to all 32 datasets available via this dataset (including the training and testing data sets), and the results were submitted to the organizers for extracting the evaluation parameters. Table 1 gives the summary of the evaluation parameters obtained: OV that quantifies the tracking/overlap of the complete vessel as annotated by the human experts, OT that quantifies the tracking of the portion of the vessel that is assigned to be clinically relevant by experts, OF that quantifies the tracking of a coronary artery until the first error and AI, an accuracy measure of centerline extraction, which is the average of all the connections between the ground truth and the extracted centerline. We observe that the framework yields comparable results to the methods evaluated in [77], which also provides more detailed definitions of the evaluation parameters employed in this work. Also, we note that the proposed framework fits into Category 3 of evaluated methods as per the classification of [77] since we use more than one input point for the vessel segmentation from this data set (an average of 3-5 input points are employed per subject for this data

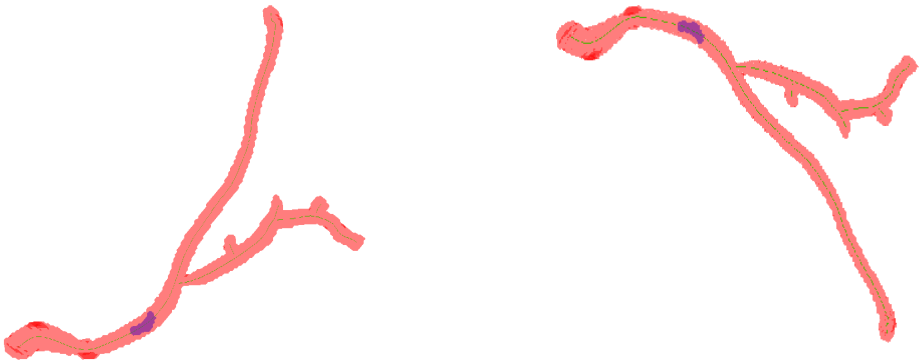

Figure 10: 3D Visualization of the vessel tree for Case 1: segmentation result (red), center-line (green), initialization (blue)

set). Finally, we note that along with yielding good performance, the proposed method also compares favorably with the methods evaluated in [77], notably in not needing to be trained for its use in the segmentation of real data along with its use of a limited number of initial points. Further, as compared to the other methods, the proposed framework simultaneously detects both the volume in 3D as well as the center-line of the vessel structure. Figures 16 and 17 show visualizations for the results of 2 cases from this dataset.

A potential application of our framework is stenosis evaluation. Since the 3D skeleton and the associated radius function are direct outputs of the model, we can do a stenosis evaluation by looking for local minima of the radius function along the center-line. We show proof-of-concept of this idea in Figure 15 which shows the cross-sectional area of one of the branches of the extracted vessel tree shown in Figure 10 and reveals a site of mild stenosis (40% blockage) (corresponding to the minimum of the plotted curve).

2.5 Concluding remarks on the tubular tree segmentation framework

In this chapter, we presented a novel framework for extracting tubular, branched anatomical structures that *simultaneously returns the segmented volume and the 3D skeleton of the structure of interest*. We showed that our methodology is successful in segmenting structures of interest from imagery of different modalities especially on the Cingulum Bundle

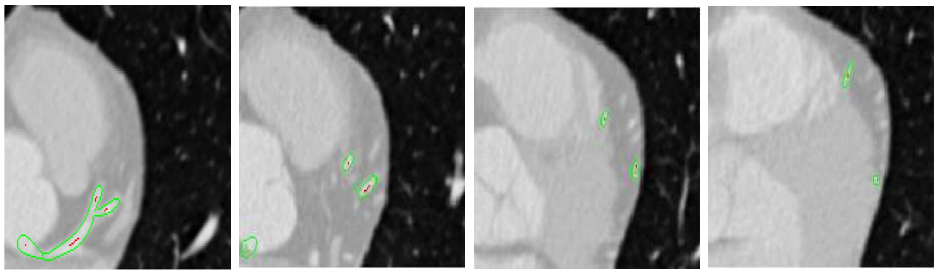

Figure 11: Slicewise views of the vessel segmentation result for Case 1

Figure 12: 3D Visualization of the vessel tree for Case 2: segmentation result (red), centerline (green), initialization (blue)

from DW-MRI of the brain and blood vessels from cardiac CTA imagery. We demonstrated the generality of the framework by applying it to the segmentation of other neural fiber bundles (the Internal Capsule and the External Capsule). We also proposed an automatic branch detection algorithm which we have successfully applied to the segmentation of entire blood vessel trees. The incorporation of local region-based statistics implies that the segmentation result captures regions with statistics that can differ over the length of the entire structure. This is clearly illustrated by the performance of the framework in capturing the entire CB where diffusion patterns vary along the length of the tube, and again in segmenting the entire length of blood vessels where the contrast varies along each vessel. Further, the model affords us the advantage of computational efficiency over conventional surface representations.

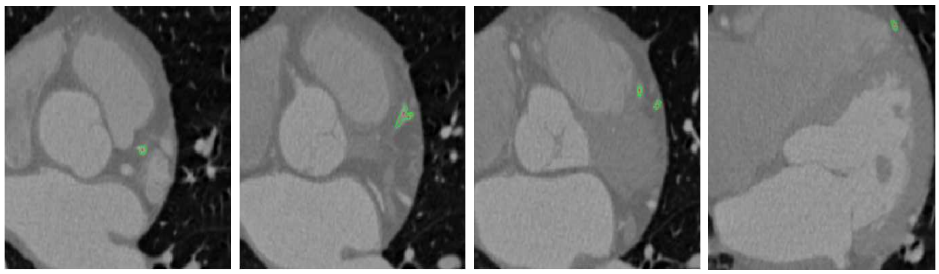

Figure 13: Slicewise views of the vessel segmentation result for Case 2

Figure 14: Visualization of the evolving tubular tree in 3D for Case 3: evolving volume (red), center-line (blue). Note that the framework captures the entire length ~ 200 voxels of the vessel starting from a simple initialization.

In future work, it would be of interest to apply the framework into segmenting other tubular anatomical structures such as carotids in the brain, and veins in the liver region, and also study in greater detail the other neural fiber bundles. Further, with respect to the analysis of blood vessels, it would be worthwhile to explore the potential of the proposed framework for soft plaque detection and particularly as a tool in evaluating stenoses.

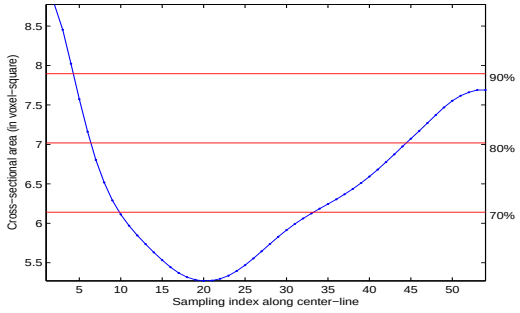

Figure 15: Cross-sectional area along vessel shown in Figure 10. The left y-axis shows the cross-sectional area in voxel-square and the red lines highlight the values of area that correspond to stenosis percentages displayed on the right y-axis. Note that the minimum of this curve indicates area of mild stenosis.

Table 1: Summary of quantitative validation results on CTA cardiac data from the Rotterdam Coronary Artery Algorithm Evaluation Framework [77] *(*it is desirable to have a high value of evaluation parameters OV, OF , OT and AI, and a low value of rank)

Measure	**% / mm**			**score**			**rank**		
	min.	**max.**	**avg.**	**min.**	**max.**	**avg.**	**min.**	**max.**	**avg.**
OV	52.8%	100.0%	91.1%	28.0	100.0	53.3	1	16	8.73
OF	4.6%	100.0%	65.3%	2.3	100.0	41.9	1	16	8.15
OT	52.8%	100.0%	92.2%	26.5	100.0	53.9	1	16	8.83
AI	0.25 mm	0.93 mm	0.47 mm	12.4	48.8	24.8	5	16	12.90
Total							**1**	**16**	**10.73**

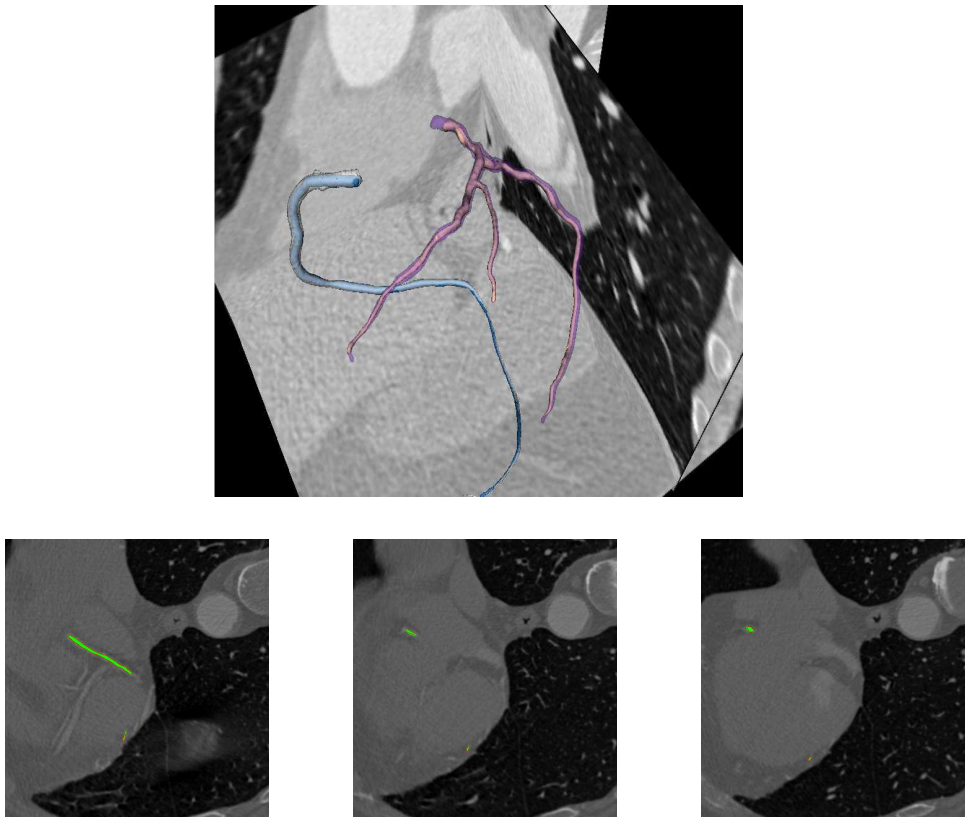

Figure 16: Visualization of results from experiments for quantitative validation using the Rotterdam cardiac data set [77] (Sample case 1): Top row shows 3D visualization with ground truth (blue and peach) and corresponding vessel trees segmented by proposed framework (white and magenta), bottom row shows slice-wise visualizations of extracted vessel tree (green) and ground truth (red outline) superimposed on the CTA data

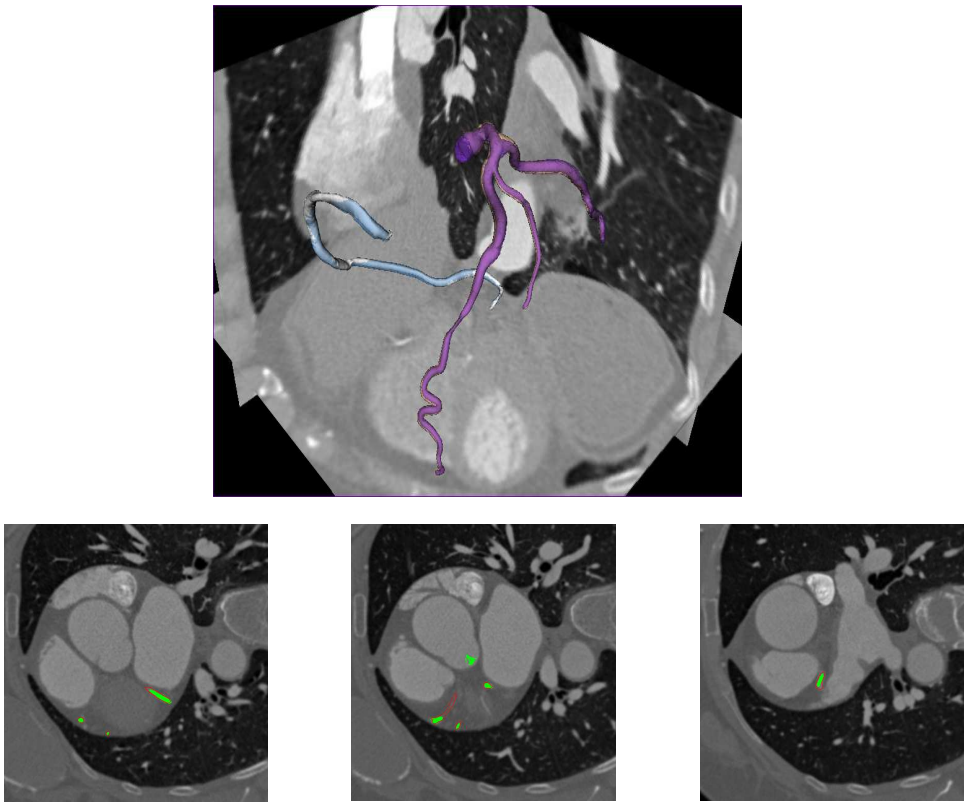

Figure 17: Visualization of results from experiments for quantitative validation using the Rotterdam cardiac data set [77] (Sample case 2): Top row shows 3D visualization with ground truth (blue and peach) and corresponding vessel trees segmented by proposed framework (white and magenta), bottom row shows slice-wise visualizations of extracted vessel tree (green) and ground truth (red outline) superimposed on the CTA data

CHAPTER III

GROUP STUDIES IN SCHIZOPHRENIA DETECTION, USING THE TUBULAR SURFACE MODEL

3.1 Motivation

Schizophrenia is a brain disorder that involves a broad range of functional disturbances, including attention, memory, emotion, motivation, thought and language, social functioning, and mood regulation. A significant body of work [25, 37, 7] supports the speculation that functional abnormalities in schizophrenia might be caused by disruptions of white matter (WM) connections. Also, several aspects of behavior associated with Cingulate Gyrus (CG) function such as attentional processing,memory, motivation and emotion, have been implicated in Schizophrenia making the study of the CG significant and since the proper functioning of the CG depends on its connections with other parts of the neuronal network, the study of the WM interconnecting the CG and other parts of the human brain is crucial.

We propose a novel framework for population analysis of DW-MRI data using the Tubular Surface Model. To begin with, we focus on the Cingulum Bundle (CB) - a major tract for the Limbic System and the main connection of the CG (though the proposed framework is equally applicable to other fiber bundles in the brain). Our model represents a tubular surface as a center-line with an associated radius function. It provides a natural way to sample statistics along the length of the fiber bundle and reduces the registration of fiber bundle surfaces to that of 4D curves. Clinical studies aimed at detection of schizophrenia have typically focused on using statistics in a volumetric analysis framework, or along individual fiber tracts [22] (which requires co-registration of the multiple fiber tracts from different subjects). In this work, we compare statistics along the length of the fiber bundles which allows us to both look for local differences and also better address the classical DWI

issues of noise and low resolution since we don't look along individual fibers.

3.2 Prior Work on Group Studies in Schizophrenia Detection

Several aspects of behavior associated with Cingulate Gyrus (CG) function such as attentional processing and emotion, are implicated in Schizophrenia making it significant to study the CG. CG abnormalities include bilateral CG volume and density reduction in voxel-based morphometric studies. Volume deficits in structural MRI studies have also been (albeit inconsistently) associated with hallucinations, reduced executive functions, psychomotor poverty and negative symptoms. The proper functioning of the CG depends on connections with other parts of the neuronal network, rather than simply its structure alone. A significant body of work [25, 37, 7] supports the speculation that functional abnormalities in schizophrenia might be caused by disruptions of white matter (WM) connections, and it is of great clinical interest to develop robust quantitative methods to further study this hypothesis. The CG itself connects to other brain regions via two major tracts - the Cingulum Bundle (CB) and the Uncinate Fasciculus (UF). Several symptoms of schizophrenia, including paranoia, hallucinations, and delusions, have been linked to a disruption in frontal and anterior temporal regions traveling through the UF and CB. Moreover, these tracts are involved in deficits in executive attention, memory encoding, declarative-episodic verbal memory, as well as verbal and visual memory. The study of these two fiber bundles is therefore believed to be key to understanding schizophrenia.

Diffusion Tensor Imaging (DTI) has become the modality of choice for studying WM properties. Many approaches exist in the literature for DTI processing towards Schizophrenia discrimination motivated by the increasing evidence in the literature for WM abnormalities in Schizophrenia [25, 83, 100] supporting the hypothesis of Friston et al [33] regarding disordered connectivity between brain regions in Schizophrenia. One set of methods looks into finding WM deficits associated directly with the disease, by studying Fractional Anisotropy (FA) and Apparent Diffusion Coefficient (ADC). Caprihan et al [12] used a

voxel-based strategy and applied Discriminatory PCA (DPCA) to Fractional Anisotropy (FA) measurements to discriminate between schizophrenic and normal controls. Goodlett et al [36] performed statistical comparison of fiber bundle diffusion properties between populations of DTI images, by using permutation testing based on the Hotelling T^2 statistic (for studying neurodevelopment). Park et al [72] studied hemispherical WM asymmetries by a statistical comparison of normalized FA images and the flipped images (of FA), and found evidence of asymmetry in anisotropy patterns between healthy and schizophrenic subjects. A second set of methods looks into studying the correlation of WM properties with specific symptoms and symptom groups rather than outright diagnosis alone, since it is observed that symptom profiles can vary significantly between subjects in Schizophrenia. Skelly el al [79] compared FA between schizophrenic and normal controls and performed a voxel-wise correlational analysis with the subjects' Positive and Negative Symptoms Scales (PANSS). Fujiwara et al [34] studied abnormalities in the CB (anterior and posterior) and their correlation with the psychopathology of schizophrenia, via a correlation analysis of FA with PANSS scores. Maddah et al [58] reports findings on differences in FA along the genu and bilaterally in the splenium along with increased eigen value in the Uncinate Fasciculus for schizophrenia, using their tract-oriented analysis framework described in [57].

The method proposed in this chapter attempts to bridge these two categories by providing a comprehensive method that allows an analysis with respect to the diagnosis as well as a characterization of regional involvement in the disorder by using both diagnosis as well as scales of scores such as PANSS. Further, to our knowledge, this is the first group study that uses DW-MRI data directly (for segmentation) without imposing the elliptical constraint associated with tensor estimation. Also, by the very nature of the model used for the CB, we are better equipped to evaluate its different spatial regions for abnormalities caused by Schizophrenia. The work of Fujiwara et al [34] and Wang et al [90] were steps in the direction of determining local differences in Schizophrenia and the work in this chapter aims to move along this direction. Both these studies focused on dividing the CB into 2

regions - anterior and posterior, while our framework allows for subdividing the CB into as many regions for analysis as desired, while balancing for the loss of information that would result from considering too few regions, against the loss of utility from considering too many regions along the white matter structure.

3.3 Population Analysis Framework

In the proposed framework, we use the Tubular Surface Model to segment the Cingulum Bundle (CB) from the DWI images. We then build feature vectors by sampling features along the length of the CB and perform statistical analysis on these feature vectors after registering them. In this section, we first present the mathematical enhancements that allow the tubular surface model to be used in an elegant population/group study framework. We then discuss the details of feature selection, coregistration and statistical analysis.

3.3.1 Application of the model in population studies

The Tubular Surface Model affords a natural way to compare fiber bundles since the parametric representation of the surface in 3D as a curve in 4D allows the sampling of features along the length of the tubular surface. Further, the problem of registering surfaces is reduced to one of registering curves. In order to perform population studies using the model, we need co-registration of the feature vectors formed from the tubular surfaces. Towards this objective, we define three operations on the tube in our model: average tube, average of functions defined on/around the the boundary of the tube, and the distance between a (sample) tube and the average tube.

We define an average tube as represented by a center-line, $\hat{c}$ and $\hat{r}$, with $\hat{c}$ as:

$$\hat{c}, \{\phi_i\}_{i=1}^N = \arg\min_{\hat{c}, \{\phi_i\}_{i=1}^N} \sum_{i=1}^N \int_0^1 |K_{\hat{c}}(\hat{s}(\phi_i(u))) - K_{c_i}(u)|^2 \, \mathrm{d}u; \tag{19}$$

we have the following constraint on reparameterizations $\phi_i : [0,1] \rightarrow [0,1]$:

$$\phi_i(0) = 0, \phi_i(1) = 1, \text{ and } \phi_i' > 0 \tag{20}$$

that is, ϕ_i are monotone diffeomorphisms. Above, $\hat{s}$ is the arclength function of $\hat{c}$. In (19), $K_c : [0,1] \rightarrow \mathbb{R}^n$ ($n \geq 1$) is a pointwise "feature" vector of the curve c. In this paper, the CB representations were aligned length-wise under the assumption that the different regions of the CB occupied the same intervals of length along the CB in all subjects. (Alternate criteria for registration are being explored in future work.)

From the correspondence functions ϕ_i, we define an average radius function $\hat{r}$ as:

$$\hat{r}(\hat{s}) = \frac{1}{N} \sum_{i=1}^{N} r_i \circ \phi_i^{-1}(\hat{s}) \tag{21}$$

We also use the correspondence functions, ϕ_i, to pullback functions from the tubes represented by (c_i, r_i) to the average tubular structure. Let $F : \mathbb{R}^3 XR \rightarrow \mathbb{R}^M$ ($M \geq 1$) be some function defined on $\mathbb{R}^3$ (and in particular inside the tube). We consider the function as being defined along the curve in 4D and we define the average function $\hat{F}$ as:

$$\hat{F}(\hat{c}, \hat{r}) = \frac{1}{N} \sum_{i=1}^{N} F_i(\hat{c} \circ \phi_i^{-1}(\hat{s}), \hat{r} \circ \phi_i^{-1}(\hat{s})) \tag{22}$$

We also define the corresponding standard deviation function as:

$$\sigma_F^2(\hat{c}, \hat{r}) = \frac{1}{N} \sum_{i=1}^{N} \| F_i(\hat{c} \circ \phi_i^{-1}(\hat{s}), \hat{r} \circ \phi_i^{-1}(\hat{s})) - \hat{F}(\hat{c}, \hat{r}) \|^2 \tag{23}$$

Finally, to find the distance between the average $\hat{F}$ and a new test function F_t defined on a tubular surface (c_t,r_t) , we find a correspondence as:

$$\phi_t = \arg\min_{\phi_t} \int_0^1 |K_{\hat{c}}(\hat{s}(\phi_t(u))) - K_{c_t}(u)|^2 \, \mathrm{d}u, \tag{24}$$

and then we can define a distance between functions:

$$d(\{\hat{F}, \hat{c}, \hat{r}\}, \{F_t, c_t, r_t\}) = \int_0^1 \| \hat{F}(\hat{c}(\hat{s}), \hat{r}(\hat{s})) - F_t(c_t \circ \phi_t^{-1}(\hat{s}), r_t \circ \phi_t^{-1}(\hat{s})) \|^2 \, \mathrm{d}\hat{s} \tag{25}$$

3.3.2 Feature Extraction

We propose to use the following features to describe the CB: mean curvature, geometric curvature, normalized cross-sectional area, center-shifted coordinates (as defined in [53]),

Fractional Anisotropy (FA) and Mean Diffusion (MD). FA and MD characterize the WM properties while mean curvature, geometric curvature and the center-shifted coordinates encode shape information. The normalized cross-sectional area incorporates the thickness of the WM connections. Note that this usage of a combination of features is a significant improvement over prior approaches (E.g. [22, 12]) which fundamentally employed only WM properties such as FA in a volumetric analysis framework. Further, while we sample along the center-line, the features are in fact extracted over the entire fiber bundle volume and hence this choice of sampling while facilitating registration, does not reduce the statistical power of our results. Finally, besides using a combination of these features for classification, we also compare their discrimination ability, which allows us to make inferences about which feature (or combination thereof) are the most useful with regard to the study of schizophrenia.

3.3.3 Coregistration

In order to perform population studies using the model, we need co-registration of the feature vectors formed from the tubular surfaces. Towards this objective, we first define three operations on the tube in our model: average tube, average of functions defined on/around the the boundary of the tube, and the distance between a (sample) tube and the average tube, all of which are described in detail in Section 3.3.1.

We then define two schemes for coregistering the segmented neural fiber bundles.

In the first scheme, we use the arc length measure along the center-line to register two fiber bundles. The corresponding reparametrization $\phi_i : [0,1] \rightarrow [0,1]$ is defined as:

$$\phi_i(s) = s \tag{26}$$

In the second scheme, we again use the arc length measure along the center-line however we register two given fiber bundles within defined regions of interest. The reparametrization $\phi_i : [0,1] \rightarrow [0,1]$ corresponding to this scheme is defined as:

$$\phi_i(s) = s_1^t + \frac{s_2^t - s_1^t}{s_2^o - s_1^o}(s - s_1^o) \tag{27}$$

where s_1^o, s_2^o and s_1^t, s_2^t are the beginning and ending lengths for a specific region of interest, for the origin fiber bundle and the target fiber bundle respectively.

It is to be noted that the first reparameterization scheme is proposed as the most intuitive scheme for registering fiber bundles from different subjects, since it naturally handles the varying lengths of the bundles caused by the different brain dimensions and anatomy. However it is observed with neural fiber bundles that when experts mark ROIs, these ROIs can be used for registration of neural fiber bundles since observations made about the relative involvement of different *regions* in the disorder can be correlated to regions that are anatomically of significance. The second scheme is then proposed as an extension of the first scheme, to address the need of localizing the effects of schizophrenia with respect to region, when markings for such regions are available.

3.3.4 Statistical Analysis - Classification

The classification step in this work has the twin goals of robust discrimination between schizophrenic and normal controls, and also of characterizing the discrimination ability of the different spatial regions of the CB. In this section, we discuss the methods employed under the classification section. We perform two sets of classification analyses - supervised classification using neural networks and unsupervised classification (clustering) using the k-means algorithm. In this work, towards performing supervised classification using an Artificial Neural Network, we use the Neural Network toolbox of MATLAB [26] to build and train a simple feed-forward Backpropagation network with 1 hidden layer (having 5 neurons). The classification results obtained using the same are provide under the results section 3.4.2. The second technique is unsupervised classification (clustering). The goal for applying clustering techniques in the context of this work is to detect natural clusters in the feature data extracted, and validate the results from the supervised classification to ensure robustness (details in Section 3.4.1). In this work, we perform clustering using the K-means algorithm [41, 38] with a target of 2 clusters.

3.3.5 Statistical Analysis - Characterization of discrimination ability

We perform two sets of statistical analyses aimed at characterizing the discrimination ability of the local regions of the CB - t-statistical tests and a correlational analysis of the extracted features with the symptom scores (PANSS) versus simply the diagnosis.

The t-statistical tests are aimed fundamentally at characterizing the spatial variation in discrimination ability. Since we build multiple features at each sample point along the center-line of the tubular surface, we estimate t-statistics with respect to all these features, and subsequently scale each category of features and sum the t-statistics for all features at each point, to get a comprehensive estimate of the t-statistic in a spatial sense. They also allow us to compare the discrimination ability of different categories of features such as shape information versus FA. In correlational analysis, we look at the correlation coefficients for the extracted features along the length of the bundle, with respect to the positive and negative symptom scores (the PANSS scale). This allows us to interpret regions with higher correlation with the symptom scores as being significant in Schizophrenia.

3.4 Experiments and Results

The population study using the framework proposed in this chapter, was carried out in two stages - the first with a limited population of 20 subjects and the second stage involving the extension of the framework to a larger population of 54 subjects. The results from both sets of experiments are given here in for comparison, and to build towards the discussion and comments thereafter on the generalization of population study results.

3.4.1 Data

The DWI imagery used in this work was acquired on a 3T magnet using an echo planar imaging (EPI) DTI Tensor sequence with a double echo option to reduce eddy-current related distortions (Heid 2000; Alexander 1997). The data was acquired in 51 directions with b=900, 8 baseline scans with b=0. Scan parameters are: TR 17000 ms, TE 78 ms,

Table 2: Local peaks of discrimination ability

CB region	T-value (Left, local maximum)	T-value (Right, local maximum)
Anterior	4.643	4.372
Posterior	5.529	5.886

Table 3: Classification performance

Classification method	Type	Side	Classification Accuracy	Sensitivity	Specifivity
Neural networks	Supervised	Left	100%	90%	96%
Neural networks	Supervised	Right	100%	90%	94%
K-means	Unsupervised	Left	78%	83%	71%
K-means	Unsupervised	Right	75%	80%	69%

FOV 24 cm, 144x144 encoding steps, 1.7 mm slice thickness. 85 axial slices were acquired parallel to the AC-PC line covering the whole brain. The population analyzed in the first stage comprised 20 male subjects - 10 normal controls and 10 schizophrenic - spanning the age group of 21-55 years (mean of ~ 43 years).

3.4.2 Results

As discussed previously, we use the tubular surface framework of Chapter 2 to segment the Cingulum Bundle (CB) from the 20 data sets in the population under study. We extract feature vectors as described in Section 3.3.2 and register the same using Equations 19,21,22 and 23, using the coregistration scheme of Equation 26. Figure 18 shows the t-statistics visualized over the fiber bundle surface for both the right and left CB, separated by feature. We can see a correlation in the spatial patterns evidenced by the FA, Mean Diffusion and cross-sectional area. Interestingly, while the center-shifted coordinates highlight multiple regions of the CB as being significant, we do see that the spatial patterns shown by the geometric curvature correlate with those of the diffusion-related features.

Figure 19 shows us a consolidated view of the spatial t-statistics (with all features equally weighted). We can see clearly that this visualization highlights regions that are

most significant in Schizophrenia classification (in red) allowing us to probe for anatomical explanations of the relevance of these specific regions. Note that the model allows us to subdivide the CB into as many subregions as desired for study, however in this work, we have divided it simply into anterior and posterior regions as a proof-of-concept and we include these statistics in Table 2. The results of the experiments on classification are summarized in Table 3. We obtained excellent classification with Neural Networks. Given the size of the population under study, to address the potential concern of over-fitting, we also conducted unsupervised clustering. We obtained promising results on the feature space discussed in this work, and are pursuing both the use of a larger population for increased robustness of the results, as well as additional features to describe the CB so as to enhance natural clusters. Note that the sensitivity and specificity reported in Table 3 were estimated using a Leave-two-out validation strategy for the Neural Network. To estimate comparable metrics for the K-means algorithm, we "classified" two data sets at a time using the clusters obtained for the remaining 18 data sets.

Finally, we performed correlational analysis on the extracted features towards understanding their relationship to the symptom scores (versus simply the diagnosis) and the results of this analysis are summarized in Tables 4 and 5. We use here the PANSS scores of the 10 schizophrenic cases in the data set under study and the CB is divided into 6 regions (ordered from anterior to posterior) corresponding to gray matter regions identified by expert marking: Rostral anterior cingulate, Caudal anterior cingulate, Posterior cingulate, Isthmus cingulate, Parahippocampal gyrus and Entorhinal cortex. The correlational analysis reveals some interesting results in that the Rostral anterior cingulate (RAC) is identified most consistently as the most significant region along the CB fiber bundle volume with respect to involvement in Schizophrenia (by way of correlation with PANSS scores as represented by the correlation coefficient). The identification of the anterior region as being significant in Schizophrenia is consistent with the observations made in prior work [5, 34, 90] and our method allows us to further localize the region of interest to the RAC.

Table 4: Correlational Analysis (with PANSS positive symptom scores)

Feature	Mean correlation coefficient (L)	Mean correlation coefficient (R)	Maximum correlation coefficient (L)	Maximum correlation coefficient (R)	Region with maximum correlation coefficient (L)	Region with maximum correlation coefficient (R)	Significant Region (combining left and right sides)
Mean Curvature	0.8077	0.8078	0.9079	0.9062	RAC	RAC	RAC
Geometric Curvature	0.7261	0.7230	0.9450	0.8794	RAC	RAC	RAC
Center-shifted coordinates	0.4529	0.4778	0.6692	0.9146	RAC	RAC	RAC
Fractional Anisotropy	0.7920	0.7957	0.9412	0.9545	PC	PC	PC
Mean Diffusion	0.8100	0.8096	0.9094	0.9139	PC	PC	PC
Cross-sectional area	0.7094	0.6506	0.8957	0.8308	RAC	CAC	CAC
Bucket-of-features	-	-	-	-	RAC	RAC	RAC

RAC - Rostral anterior cingulate; CAC - Caudal anterior cingulate; PC - Posterior cingulate

For a more detailed discussion on PANSS scores, the interested reader is referred to the work of Kay et al [42].

3.4.3 Results with extended population

A key consideration in performing population studies aimed at disorder detection is the extent of generalization of the observed results, that is the certainty that the observed patterns will be found in new data from previously unseen subjects. Increasing the size of the population used for training is a reliable way to ensure good generalization of results, and towards that goal, in the second stage of experiments, the proposed framework was applied to a population of 54 subjects (27 normal control and 27 schizophrenic). The classification results from this population are summarized in Table 6.

Table 5: Correlational Analysis (with PANSS negative symptom scores)

Feature	Mean correlation coefficient (L)	Mean correlation coefficient (R)	Maximum correlation coefficient (L)	Maximum correlation coefficient (R)	Region with maximum correlation coefficient (L)	Region with maximum correlation coefficient (R)	Significant Region (combining left and right sides)
Mean Curvature	0.7335	0.7348	0.8415	0.8440	RAC	RAC	RAC
Geometric Curvature	0.6589	0.6569	0.8637	0.8276	RAC	RAC	RAC
Center-shifted coordinates	0.3855	0.3538	0.6690	0.5826	RAC	RAC	RAC
Fractional Anisotropy	0.7157	0.7195	0.8917	0.8674	PC	PC	PC
Mean Diffusion	0.7362	0.7355	0.8519	0.8494	RAC	RAC	RAC
Cross-sectional area	0.6862	0.6235	0.8847	0.8141	CAC	CAC	CAC
Bucket-of-features	-	-	-	-	RAC	RAC	RAC

RAC - Rostral anterior cingulate; CAC - Caudal anterior cingulate; PC - Posterior cingulate

Table 6: Classification performance on the extended population

Classification method	Co-registration	Side	Classification Accuracy	Sensitivity	Specifivity
Neural networks	Using arc length	Left	50.6%	51.4%	64.6%
Neural networks	Using arc length	Right	50.7%	55.8%	39.4%
Neural networks	Using ROI	Left	50.6%	44.6%	66.4%
Neural networks	Using ROI	Right	48.3%	55.6%	29.7%

3.4.4 Discussion of results

We note from Table 6 that on extension to the larger population, the classification performance of the proposed framework as applied to the Cingulum Bundle does not generalize in a manner that would conclusively allow us to apply the results in the detection of schizophrenia from data of previously unseen subjects. Given prior work that supports the hypothesis that the white matter structures (including the Cingulum Bundle) display variations in shape and diffusion properties under schizophrenia, it is of interest to understand this performance of the framework.

The first observation comes from comparing the segmentation framework used in this framework to the streamlining-based tractography approaches. We note that the tubular surface segmentation framework proposed in this thesis captures the white matter bundle by growing out an initial *tube* in the primary direction of diffusion of water molecules. As a result, we note that the framework captures bundles upto a crosssection that contains strongly diffusing voxels while streamlining-based approaches also pick up voxels with less-strong diffusion characteristics, and hence discriminate between schizophrenic and normal controls on that feature.

The second observation is that in the experiments presented in this thesis, we have focused on the cingulum bundle, while other studies in schizophrenia detection have also included other white matter structures including the corpus callosum and the uncinate fasciculus among others. It is hence important to also apply the the framework to other white matter structures to truly leverage its usefulness in schizophrenia detection.

The third observation is with regards to the classification technique. Since neural networks and k-means both innately assume linear separability in the data under analysis, it might be a worthwhile extension to utilize nonlinear techniques such as kernel-PCA and this is a key direction for future research on this front.

3.5 Concluding remarks on population studies towards schizophrenia detection

In this chapter, we propose a novel framework for population analysis of neural fiber bundles that utilizes the tubular surface model proposed in Chapter 2 for extracting and representing the fiber bundle under study. The framework facilitates the statistical analysis towards the dual goals of classification and characterization of discrimination ability by region. In this chapter, we focus on the application of the framework to the cingulum bundle and demonstrate via two stages of experiments, its ability to detect differences, its output with regard to characterizing the role of different regions in the disorder under study, and most importantly discuss factors that influence the robustness and generalization of the results obtained. We obtain excellent classification using Neural Networks, and are able to verify natural clusters in the feature data by use of the K-means algorithm, in the first stage of experiments and subsequently observe in the second stage that while the data still displays some natural clustering, it longer yields the same classification performance, an observation that we seek to explain via inferences about the choice of classification technique and the white matter structures under study. Using t-statistical tests and correlation analysis, we demonstrate how the framework naturally characterizes the discrimination ability of different regions of the Cingulum Bundle in Schizophrenia and helps provide insight into the involvement of different regions in the disorder. This is a useful application of this framework that is relevant across different population sizes used for analysis. Extending the study to other white matter structures, coupling with competing techniques such as streamlining-based tractography, and using nonlinear techniques such as kernel-PCA in classification are some key directions to be pursued for future research on this front.

(a) Mean Curvature

(b) Geometric Curvature

(c) Center-shifted coordinates

(d) FA

(e) Mean Diffusion

(f) Crosssectional area

Figure 18: Visualization of t-statistics (by feature) on Cingulum Bundle surface (discrimination ability increases from green to red regions)

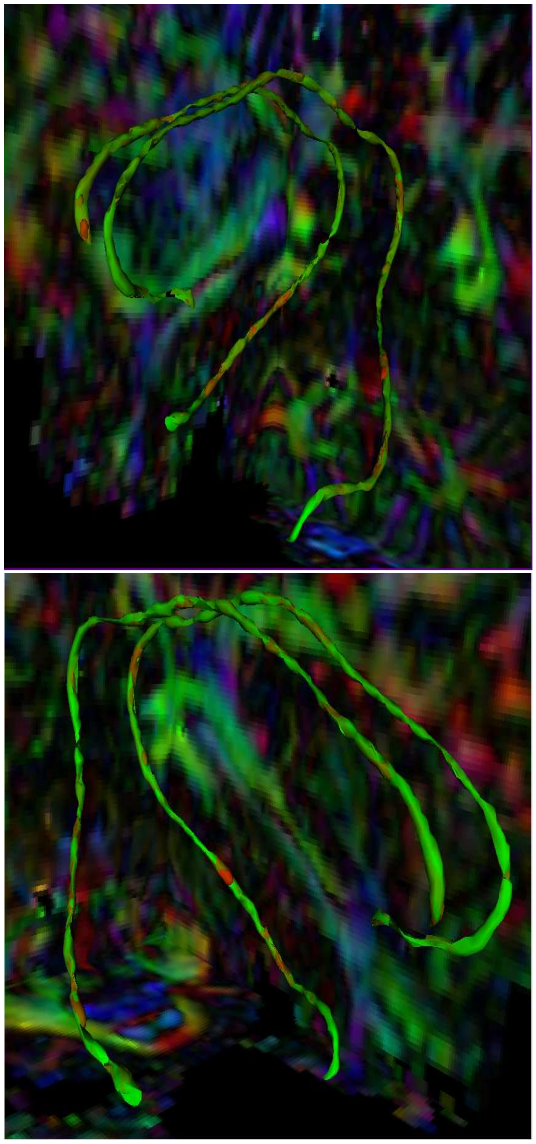

Figure 19: Visualization of t-statistics (consolidated) on Cingulum Bundle surface, overlaid on DTI data of one subject (discrimination ability increases from green to red regions)

CHAPTER IV

ANALYSIS OF MASS SPECTROMETRY IMAGING

This chapter discusses the research topic on the analysis of Mass Spectrometry Imaging (MSI), specifically as focused towards the goal of integrating MSI into the surgical workflow as an intraoperative imaging modality. There are two broad applications we aim to address in the context of MSI analysis - classification of tissue samples (into tumor types) using MSI, and estimation of tumor boundary locations using MSI. We address each of these research problems in the respective dedicated sections of this chapter, i.e. Sections 4.3 and 4.4.

4.1 Motivation

The World Health Organization (WHO) recognizes over 125 types of brain tumors based on histopathological evaluation, and classifies them according to cellular characteristics, and grades malignancy by proliferation, cellular and nuclear morphology, vascularization, and certain biomarkers. Gliomas are the most common human primary brain tumors, with astrocytomas comprising the most common subtype ranging in grade from WHO grade II to the most aggressive form, gliobastoma multiforme (grade IV). The current state of the art in the diagnosis and grading of gliomas is based on neuropathological examination of a biopsy sample and characteristic cytogenetic aberrations [93], along with radiographic imagery to characterize the tumor anatomy (size, location, etc.), and its relation to the surrounding healthy tissue. However, histopathological evaluation of tissue is of limited use in surgical intervention since it needs expert evaluation of tissue resected from the tissues of interest. Hence, during surgery, traditional pathology-based approaches need to be complemented by intraoperative detection of tumors complete with tumor classification and tumor boundary location. Further, this intraoperative detection is required to not interfere

with the normal surgical workflow. Conventional imaging modalities pose challenges with regard to their usefulness in intraoperative situations where the structures tend to shift and change, and hence this motivates the use of alternate modalities such as Mass Spectrometry Imaging.

Mass spectrometry is a well established analytical technique used for the identification and characterization of molecules based upon their accurate mass. With the recent adaptation of mass spectrometers to accommodate direct tissue analysis, an increasing number of studies support the usage of mass spectrometry as an efficient tool to detect and delineate pathology directly from tissue specimens [11, 14]. In 2004, Desorption ElectroSpray Ionization (DESI) was introduced as an atmospheric pressure ionization source and subsequently proven to be applicable to tissue imaging [84, 20, 96]. In addition to being a soft ionization method that allows the analysis of intact biomolecules, DESI provides direct sampling of the surface of interest, overcoming time and quality limitations that normally result from specialized sample preparation. This technique paves the way for the integration of Mass Spectrometry into the clinical environment (which is the theme of the proposed research) for in vivo molecular imaging of tumors, without the systemic injection of contrast agents.

Figure 20 gives an idea of the surgical tool that is the final desired outcome of this overall research. The relative intensities in the vicinity of each peak under analysis for each of the samples were analyzed and the values scaled to fit the range 0-255 corresponding to the color scale and we then use the RGB format to render the coloring in Slicer3, an open-source visualization tool provided by the NAMIC consortium. Green to red indicates an increasing relative intensity corresponding to the m/z value. The sites were sized by the true radius of the samples, scaled to the size of the brain imagery used, and InstaTrak common figure for accuracy is 2.28 mm, i.e. mean accuracy of the whole system (registration and tracking) which we round to a radius of 2 mm for all sites except site 8, which we visualize with a radius of 8 mm corresponding to its volume of acquisition. Similar visualization

of the tumor cell concentration is presented with the 0-255 color scale corresponding to 0-95% tumor cell concentration as scored by expert neuropathology evaluation of permanent tissue sections.

A major portion of brain tissue is made up of lipids, and altered levels of lipids in brain tissue are correlated with several diseases such as Alzheimer's, neuronal ceroid-lipfuscinosis and cancer. Especially relevant to this work, altered lipid levels have been reported in human gliomas [44, 6]. Thus, lipids can act as biomarkers for disease, reflecting the histopathological cell type, state of cellular growth, maturation and differentiation of a cell. Mass Spectrometry (MS) imaging is an excellent candidate to assist in intra-operative decision making since the technique yields detailed chemical information about samples, and the development of an ambient acquisition technique such as Desorption ElectroSpray Ionization (DESI) enables the introduction of this tool into the surgical workflow. The missing link in this integration of MS imaging into the surgical workflow, is the need for real-time quantitative analysis tools for MS imaging data. In this work, we first address the question of DESI-MS data classification (into glioma subtypes) as well as identifying suitable feature selection techniques towards the detection of biomarkers. Figure 4.3 shows the visualization of sample spectra from the analyzed dataset for all four glioma subtypes. We then consider the problem of intraoperative tumor boundary detection and motivate the mathematical framework for this problem along with a discussion of the results obtained.

4.2 Prior Work on Mass Spectrometry Imaging Analysis

Brain tumors are especially challenging to treat due to their location within the complex and delicate anatomy of the brain and their problematic biological behavior. Primary brain tumors span a large range of cell types and grades (World Health Organization (WHO) classification system [81]); moreover within individual tumors there may be considerable

heterogeneity leading to sampling error. Current diagnosis and treatment rely upon observations of tissue and cellular characteristics such as proliferation, cellular and nuclear morphology, vascularization, and limited cytogenetic profiling. Since the appropriate choice of treatment, as well as estimates of prognosis, rely upon an accurate diagnosis, current histopathological approaches need to be augmented by detailed molecular profiles from each individual's tumor to maximize treatment efficiency. Also, surgery remains the first line of treatment for most brain tumors. Moreover, there is a critical tradeoff between the extent of surgical resection (which affects the prognosis for most brain tumors) and the preservation of critical cortex and white matter (which directly correlates with brain function). There has been significant progress in developing imaging platforms for visualization of tumor pathology, critical anatomy, and functional brain areas, which have been used to guide neurosurgical interventions. However, intra-operative decision-making is still hindered by the lack of information available to the surgeon concerning tumor margins and molecular characteristics of the lesion.

In reviewing prior work in the field of the analysis of Mass Spectrometry Imaging, we find two broad classes of work as aligned with the two distinct stages in MSI analysis - the first on preprocessing and the second on statistical analysis. Preprocessing of Mass Spectrometry data includes denoising, normalization, spectral alignment and feature selection for subsequent classification analysis. An excellent comparison between various feature selection methods such as the student t-test and the P-test as well as an evaluation of dimensionality reduction techniques (such as PCA) as applied to MS data, can be found in [49]. In [21], the authors use the undecimated discrete wavelet transform to decompose mass spectra into noise and signal components, and combine this denoising step with a baseline correction towards improved peak detection, and apply this to the analysis of breast cancer data. In [69], the authors put forth a work flow view of MSI processing and illustrate the value of preprocessing particularly with regard to the benefits associated with denoising. In the second category of statistical analysis, existing literature (in

the subcontext of biomedical research) is primarily targeted at classification between multiple classes (such as malignant/ benign) or the identification of biomarkers towards the characterization/understanding of a specific disease [27]. [35] addresses the classification of MALDI-Imaging data using classical techniques such as PCA and SVMs. [97] compares various statistical methods employed in the classification of ovarian cancer from MS imagery, including discriminant analysis, k-nearest neighbor classification, SVMs and RF (Random Forest) and articulates some clear advantages for the RF category of methods. Finally, in the scope of the proposed research (to be discussed in Chapter 4), we are interested in meaningfully integrating histopathological and molecular information. While there has been prior work in integrating histology and Imaging Mass Spectrometry (for instance in [15]), it is worth noting that most of this work has been focused on the image acquistion stage, and subsequently on parallel use of the two modalities in a qualitative fashion, and a quantitative analysis framework linking these two modalities hasn t been identified. This is a key gap that this work aims to address.

We note that the majority of the existing literature when it uses histological information for analysis, primarily uses it in classification (for training in a supervised classification paradigm) or for validation of statistical frameworks. [85, 89, 3] which address classification and [27, 51] which address the identification of biomarkers towards the characterization/understanding of a disease are notable examples under this category. However, the current work falls under the combined mathematical purview of classification, feature selection and modeling. We note that prior work in the field of modeling with regard to mass spectrometry data is focused greatly in modeling mass spectra themselves as a function of time and/or *m/z*. For example, [80] puts forth a framework for efficiently pooling mass spectra by modeling the statistical properties of single-shot spectra in the framework of linear regression, which yields a maximum-likelihood estimator that is then employed in pooling at each time interval, and [54] puts forth a regression-based approach for protein expression profile modeling. Note that while these are very effective modeling approaches,

their fundamental application lies in the preprocessing of mass spectrometry data. Our interest however lies in going beyond acquisition and classification and specifically in Section 4.4, we are interested in modeling histopathological information (specifically the tumor cell concentration) as a function of mass spectra towards intraoperative applications of mass spectrometry such as tumor boundary detection, and to the best of our knowledge, this is the first work that addresses this specific modeling problem.

4.3 Classification of Tissue Samples and biomarker detection using MSI

The World Health Organization (WHO) recognizes over 125 types of brain tumors based on histopathological evaluation, and classifies them according to cellular characteristics, and grades malignancy by proliferation, cellular and nuclear morphology, vascularization, and certain biomarkers. Gliomas are the most common human primary brain tumors, with astrocytomas comprising the most common subtype ranging in grade from WHO grade II to the most aggressive form, gliobastoma multiforme (grade IV). The current state of the art in the diagnosis and grading of gliomas is based on neuropathological examination of a biopsy sample and characteristic cytogenetic aberrations [93], along with radiographic imagery to characterize the tumor anatomy (size, location, etc.), and its relation to the surrounding healthy tissue. However, histopathological evaluation of tissue is of limited use in surgical intervention since it needs expert evaluation of tissue resected from the tissues of interest. Hence, during surgery, traditional pathology-based approaches need to be complemented by intraoperative detection of tumors complete with tumor classification and tumor boundary location. Further, this intraoperative detection is required to not interfere with the normal surgical workflow.

A major portion of brain tissue is made up of lipids, and altered levels of lipids in brain tissue are correlated with several diseases such as Alzheimer's, neuronal ceroid-lipfuscinosis and cancer. Especially relevant to this work, altered lipid levels have been

reported in human gliomas [44, 6]. Thus, lipids can act as biomarkers for disease, reflecting the histopathological cell type, state of cellular growth, maturation and differentiation of a cell. Mass Spectrometry (MS) imaging is an excellent candidate to assist in intra-operative decision making since the technique yields detailed chemical information about samples, and the development of an ambient acquisition technique such as Desorption ElectroSpray Ionization (DESI) enables the introduction of this tool into the surgical workflow. The missing link in this integration of MS imaging into the surgical workflow, is the need for real-time quantitative analysis tools for MS imaging data. In this work, we specifically address the questions of DESI-MS data classification (into glioma subtypes) as well as identifying suitable feature selection techniques towards the detection of biomarkers. Figure 4.3 shows the visualization of sample spectra from the analyzed dataset for all four glioma subtypes.

In this work, we apply machine learning techniques towards the classification of the samples in a glioma data set acquired by DESI-MS imaging, into one of four subtypes of gliomas. Further, we move towards biomarker discovery using KS-statistics and the Maximum Influence Feature Selection algorithm (MIFS, which was originally proposed for the analysis of multiclass Comparative Genomic Hybridization (CGH) data in bioinformatics [55]).

4.3.1 Classification Framework

4.3.1.1 Preprocessing and Feature Selection

We explore two feature selection methods in the scope of this work: the Kolmogorov-Smirnov (KS) statistic-based feature selection, and Maximum Influence based Feaure Selection (MIFS) [55]. The KS test is a nonparametric test of equality for 1-D probability distributions, and we use it here to estimate a *distance* between the empirical distribution functions of each set of two samples (each tumor class versus the others) which allows us to compare the discrimination potential of the different mass to charge (m/z) ratio values, and

select a subset of these *m/z* as features based on p-value. We use the MATLAB Statistics Toolbox^{TM} for conducting this KS statistic-based feature selection.

The MIFS test is an iterative test to select features that provide the largest incremental increase in an objective function of discrimination (such as the objective function for the SVM used for classification). It is performed here as motivated in [55]. Since the MIFS test is performed offline, we are not concerned with performance issues, and initialize the feature list for the algorithm by selecting the m/z value that displays greatest *discrimination* for the various tumor classes as measured using the KS-statistic. As compared to [55], our implementation differed in that we retrained the SVMs at each iteration of MIFS to assess the change in objective function for each of the remaining features. While this is computationally expensive, it yielded better results with respect to overall classification using the final set of features. Again, since the MIFS algorithm is performed offline, its computational efficiency does not impact the real-time utility of the overall framework with respect to integration into a surgical workflow.

4.3.1.2 SVM-based Classification

In this work, we utilize the well-established technique of Support Vector Machines [24] for classification of the glioma samples. Prior work (such as [89]) has shown that SVMs are one of the most robust techniques with respect to mass spectrometry imaging data classification. Given a set of points in a high-dimensional space such that each point belongs to one of two classes, an SVM performs classification by estimating as a decision boundary, the hyperplane maximizing the margin separating the two classes. Thus, the basic SVM is a tool for binary classification. Since we are dealing with a multiclass classification problem in this work, there are two approaches available: to partition the overall problem into a combination of binary classification problems for each of which we can employ a SVM, or to use the approach of Crammer et al [23] to directly apply a single SVM for the multiclass problem. In the scope of this paper, we focus on using the first of these approaches. We use

a one-versus-all strategy to train multiple SVMs and combine the feature *rankings* from the multiple SVMs to obtain an overall feature ranking, which we then use in the feature selection process. We create four individual SVMs to classify each glioma class versus all the others, and finally combine the classification outputs of all four SVMs as given in Equation 28 to obtain the final classification result s_{final} as follows:

$$s_{final} = s_a\bar{s_b}\bar{s_c}\bar{s_d} + \bar{s_a}s_b\bar{s_c}\bar{s_d} + \bar{s_a}\bar{s_b}s_c\bar{s_d} + \bar{s_a}\bar{s_b}\bar{s_c}s_d \tag{28}$$

where s_a, s_b, s_c and s_d denote the outputs from the individual SVMs trained with the one-versus-all strategy for the four different subtypes (anaplastic astrocytomas, glioblastomas, oligodendrogliomas and oligoastrocytomas respectively).

4.3.2 Experiments and Results

4.3.2.1 Data

The tissue samples used in this work were obtained from the Neurooncology Program Biorepository collection at Brigham and Women's Hospital (BWH), and analyzed under approved Institutional Review Board (IRB) protocol, with informed written consent obtained by licensed neurosurgeons at BWH. The DESI ion source was a lab-built prototype, configured as described in [40]. The data set analyzed comprised 13 subjects - three each with anaplastic astrocytoma, oligodendroglioma and oligoastrocytoma, and four with glioblastoma - with multiple spectra from each for a total of 398 (profile) spectra. Each of the samples had entire mass spectrometric images (multiple mass spectra acquired across the tissue section surface), and each profile spectrum was computed as the sum of the acquisition scans from a complete row. These 398 profile spectra were then put through the analysis framework described in this work.

4.3.2.2 Experiments and Results

In the first part of this work, we applied SVMs to the classification of the glioma data, with a view to understanding the impact of preprocessing and feature selection on classification.

Table 7: Classification performance

	Number of features	Accuracy	Sensitivity	Specificity	Classification time (seconds)
Unscaled MSI, entire mass range	-	84.47%	40.00%	99.30%	0.18
Scaled MSI, entire mass range	-	92.76%	74.21%	98.95%	0.22
Scaled MSI, KS statistic-based feature selection, $\alpha = 0.10$	2247	98.16%	94.21%	99.47%	0.12
Scaled MSI, KS statistic-based feature selection, $\alpha = 0.05$	1599	99.47%	98.42%	99.82%	0.08
Scaled MSI, KS statistic-based feature selection, $\alpha = 0.02$	992	98.42%	95.26%	99.47%	0.05
Scaled MSI, KS statistic-based feature selection, $\alpha = 0.01$	704	98.29%	94.74%	99.47%	0.04
Scaled MSI, KS statistic-based feature selection (highest ranked by p-value)	25	94.34%	81.05%	98.77%	0.01
Scaled MSI, Feature selection using MIFS	25	92.99%	77.84%	98.04%	0.01

Table 8: Results of feature selection from the KS-statistic and MIFS-based methods (m/z values): results of the methods are displayed both without and with clustering (centroids are obtained by clustering the top-ranked 25 features from each method)

	Ranking	KS statistic-based feature selection	MIFS
Top ranked features (direct)	1	751.6	751.6
	2	864.7	999.9
	3	751.7	999.8
	4	751.5	990.9
	5	864.8	999.7
Centroids extracted by clustering	1	751.2	744.4
	2	788.1	839.6
	3	845.8	989.8

We focused on the values from 650-1000 m/z as motivated by the study of lipid profiles in [28]. We employed a one-versus-all strategy to partition this multiclass problem into four separate binary classification problems, and combine the classification results from the four individual SVMs using Equation 28. We compared the classification performance of a simple quadratic-kernel-based SVM on the raw data as against the scaled data with original dimensions, and scaled and dimension-reduced data (using the KS-statistic) with different thresholds for the p-value and finally with the dimension-reduced data using the features extracted by the MIFS algorithm. The results of this experiment are reported in Table 7. 10% of the available data was reserved for evaluation and the SVMs were trained on the remaining 90% of the data. The performance metrics reported were averaged over 250 random trials. We observe that feature selection greatly improves the classification performance, and also reduces classification time from 0.22 seconds for the entire mass range down to 0.01 seconds for classification using a set of 25 features. This is a great benefit from the perspective of integrating DESI-MS into the surgical workflow since this approaches real-time operation. Further, we compared the two feature selection methods by using a target of 25 features, and MIFS and KS statistic-based feature selection were found to yield comparable results.

In the second part of this work, we extended the SVM-based classification via the Maximum Influence Feature Selection algorithm with a view to extracting biomarkers for the DESI-MS glioma data set. We compare the features selected by MIFS with the features selected by the KS statistic-based test. The preliminary results of this experiment are summarized in Table 8 where we show the top ranked 5 m/z values from each method. The table also shows preliminary results of clustering to extract 3 m/z centroids from each set of peaks. The motivation for this clustering (using k-means) is to extract more meaningful masses to study since the quantitative techniques are observed to yield m/z values that are often clustered together on the m/z axis. This approach is currently being explored, but clustering is found to better highlight mass ranges with agreement between the two feature selection methods and this motivates future work on combining the two feature selection methods into one robust technique for biomarker discovery.

Finally, we show in Figure 4.3.2.2, the approach behind performing a molecular ID of m/z values selected by the MIFS algorithm via tandem mass spectrometry on the selected m/z. We show this for one selected m/z value of 750.5 (corresponding to the positive mode) which is one of the selected features.

4.3.3 Concluding remarks on MSI classification and biomarker detection

To conclude, we proposed a complete classification framework for DESI-MS data towards integrating MS imaging into the surgical workflow. We obtained excellent results in classification of glioma subtypes using SVMs with preliminary peak(/feature) selection using the Kolmogorov-Smirnov test. We also demonstrated the potential of the MIFS technique (originally proposed for CGH data analysis) for the analysis of mass spectrometry imaging, by obtaining excellent classification results using the extracted features for the SVM-based classification framework. We found that MIFS and the Kolmogorov-Smirnov test performed comparably well in classification performance, and we propose that SVM-based classification with an offline feature selection using a combination of these methods is an

excellent candidate for integration into the surgical workflow. We also motivated the application of the feature selection algorithms towards biomarker discovery and presented preliminary results on the molecular ID of one selected mass via tandem MS.

In future work, it will be of interest to further analyze the selected m/z values via the tandem MS technique in order to identify the molecules that they represent and study their role as potential biomarkers. It is also a worthy goal to understand the relation of selected features to prior work such as the lipid profiles identified in [28]. Integration of more preprocessing techniques such as denoising into the classification framework while maintaining its current real-time performance, and replacing the one-versus-all multiple SVM strategy with the multiclass SVM implementation of [23] towards a more integrated classification and biomarker identification framework, are other directions to be pursued in future work.

4.4 Tumor Boundary Detection

Surgery is the most important, and often the first treatment modality for the majority of brain tumors. In neurosurgical interventions for brain cancers, the principal challenge is to maximize the resection of tumor, while minimizing the potential for neurological deficit by preserving critical tissue. We aim to develop a real-time analysis of the tissue using mass spectrometry in conjunction with radiology for image-guided neurosurgery. A surgical probe is being integrated with an atmospheric pressure Desorption Electrospray Ionization (DESI) mass spectrometry source [84, 20] and a neuronavigation system to allow Real-Time Stereotactic Mass Spectrometry (RTSMS) analysis of surgical tissue for the molecular detection of tumor margins. Mass spectrometry is introduced as a molecular imaging approach, complementing or bypassing needs for systemic injections of molecular probes required for standard methods. In this work, we propose a framework where we use a training set of multiple subjects and build a predictive model to determine tumor cell concentration from Mass Spectrometry Imaging (MSI), towards detecting tumor margins

intraoperatively. In the absence of a physical model linking the data (profile spectra) to the output (the histopathological score), we frame the problem as one of regression using the Relevance Vector Machine (RVM) techniques of Tipping et al [86]. In Section 4.4.1, we present the theory behind the proposed framework, specifically the details on the preprocessing of the raw Mass Spectrometry data towards denoising and feature(/peak) selection, the details of the RVM-based model for the tumor cell concentration as a *function* of the spectra and the details of the implementation of the proposed framework, complete with the libraries and parameters used to obtain the results reported in this paper. In Section 4.4.2, we discuss the experiments conducted to validate the proposed framework, and present the results obtained. Finally, in Section 4.4.3, we make concluding remarks and present ideas for extending this work in the future.

In Figure 4.4, we show the stereotactic sampling sites visualized throughout the tumor for 1 subject with site markers colored by the absolute intensity values of the *m/z* 653.5834 (selected to illustrate the variance of molecular distribution in the sampling sites) and sized proportional to the true size of the samples acquired for analysis. The numbers 1 to 10 indicate the order of acquisition. Figure 24 shows a sample profile spectrum and corresponding stained tissue section.

4.4.1 Proposed Framework for Estimation of Tumor Cell Concentration

4.4.1.1 Modeling Tumor Cell Concentration

We formulate the problem of modeling the tumor cell concentration as a function of profile spectra, in the linear regression framework. We have the following requirements for the technique to be used - the ability to handle limited number of training inputs, the ability to generalize well and low computational cost. Hence, we propose to use Relevance Vector Machines (RVM) [86, 9] based regression for this problem, using a Gaussian kernel.

Let $\mathbf{x}_{(i,j)}$ denote the profile spectrum of the i-th sampling site from the j-th subject in our training population, and let $h(\mathbf{x})$ denote the tumor cell concentration of the profile

spectrum given by $\mathbf{x}$.

In the regression framework, $\mathbf{x}$ are the input vectors and the scalar target t can be written as:

$$t = h(\mathbf{x}) + \epsilon \tag{29}$$

where the error ϵ is modeled as independent zero-mean gaussian with variance σ^2.

We model $h(\mathbf{x})$ as:

$$h(\mathbf{x}) = \sum_{m=1}^{M} w_m \phi_m(\mathbf{x}), h = \phi(\mathbf{x})\mathbf{w} \tag{30}$$

By the error model assumed, we get:

$$p(t_n|\mathbf{x}_n) = N(t_n|h(\mathbf{x}_n, \mathbf{w}), \sigma^2) \tag{31}$$

Since t_n are assumed to be independent, the likelihood of the complete data set can be written as:

$$p(t|\mathbf{w}, \sigma^2) = (2\pi\sigma^2)^{\frac{-N}{2}} \exp\{\frac{-1}{2\sigma^2}\|t - \phi\mathbf{w}\|\} \tag{32}$$

By the RVM approach, here we constrain the parameters $\mathbf{w}$ by prior distributions using hyperparameters α as follows:

$$p(\mathbf{w}|\alpha) = \prod_{i=1}^{M} N(w_i|0, \alpha_i^{-1}) \tag{33}$$

Using Bayes' rule, we can write the posterior parameter distribution conditioned on the data as follows:

$$p(\mathbf{w}|t, \alpha, \sigma^2) = \frac{p(t|\mathbf{w}, \sigma^2)p(\mathbf{w}|\alpha)}{p(t|\alpha, \sigma^2)} = N(\mu, \Sigma) \tag{34}$$

where

$$\Sigma = (A + \sigma^2\Phi^T\Phi)^{-1} \tag{35}$$

$$\mu = \sigma^2\Sigma\Phi^T t \tag{36}$$

$$A = diag(\alpha_1, \alpha_2 ... \alpha_M) \tag{37}$$

Formulating the Sparse Bayesian Learning as a Type-II Maximum Likelihood procedure, we write the Marginal Likelihood as:

$$L(\alpha) = \log p(t|\alpha, \sigma^2) \tag{38}$$

$$= \frac{-1}{2}\left[N \log (2\Pi) + \log |C| + t^T C^{-1} t\right] \tag{39}$$

with

$$C = \sigma^{-2} I + \Phi A^{-1} \Phi^T \tag{40}$$

By maximizing $L(\alpha)$ with respect to α and σ, we get maximum probable estimates of the two quantities as α_{MP} and σ_{MP} respectively.

We finally obtain the predictive distribution for any new input $\mathbf{x}_{new}$ as:

$$p(t_{new}|t, \alpha_{MP}, \sigma^2_{MP}) \tag{41}$$

$$= \int p(t_{new}|\mathbf{w}, \sigma^2_{MP}) p(\mathbf{w}|t, \alpha_{MP}, \sigma^2_{MP}) d\mathbf{w}$$

$$= N(t_{new}|h_{new}, \sigma^2_{new}) \tag{42}$$

where

$$h_{new} = \mu^T_{MP} \Phi(\mathbf{x}) \tag{43}$$

$$\mu_{MP} = \sigma^{-2}_{MP} \Sigma \Phi^T t$$

$$\sigma^2_{new} = \sigma^2_{MP} + \Phi(\mathbf{x}_{new})^T \Sigma \Phi(\mathbf{x}_{new})$$

Thus, given a new profile spectrum x_{new}, we will use Equation 43 to predict the tumor cell concentration.

4.4.1.2 Preprocessing

The high dimensionality of mass spectrometry poses a challenge in the proposed framework. Firstly, since the number of samples typically available for training such a framework are limited, high dimensionality of input reduces the robustness of the *learned* model. Secondly, the dimensionality of the input directly affects the complexity of the framework. To

address these issues, we employ peak selection techniques to select the variables to regress over. We experiment with two techniques: using t-statistics and KS-statistics. We compute t-statistics (KS-statistics) with respect to the binned tumor cell concentration of the input samples (as classified by the expert as part of the histopathological evaluation). We then order the t-statistics (KS-statistics) and select the masses with highest (lowest) values of t-statistics (KS-statistics) for use in the modeling step i.e. these are the peaks at which the kernels in the model of Equation 30 are centered to begin with. The peak selection is illustrated in Figure 4.4.1.2.

4.4.1.3 Implementation

In the scope of this work, we implement the proposed framework in MATLAB in conjunction with C++ code utilizing the *Dlib* open source library [43]. The preprocessing and peak selection are performed in MATLAB and the RVM-based modeling is carried out using MEX code that employs the *Dlib* library. We use the sigmoid kernel in the RVM model.

4.4.2 Results

4.4.2.1 Data

The DESI Imaging data used for the experiments in this work was acquired from tissue specimens prepared at the Brigham and Women's Hospital, and analyzed in the Aston Laboratories at Purdue University. A lab-built prototype (configured as described in [20]) was used for the DESI ion source. The spray solvent used for the acquisition was methanol:water (50:50) with the application of a 5 kV spray voltage, the nitrogen gas pressure was 150 psi and the solvent flow rate was 1.5 L/min. 2D images were recorded consisting of arrays of pixels, with each pixel covering an area of 200 x 200 m2, and the samples were then analyzed in negative (*m/z* 150 1000) ion modes. The MS data was acquired using a LTQ linear ion trap mass spectrometer controlled by the XCalibur 2.0 software (from Thermo Fisher Scientific, San Jose, CA, USA). Spatially accurate images

were then assembled using the software Biomap (freeware). Finally, for the modeling experiments presented in this paper, five profile spectra corresponding to five different regions of each specimen were used. In all, 28 tissue samples of gliomas were used leading to 140 mass spectra as input for the modeling process. The glioma samples span different subtypes (anaplastic astrocytoma, glioblastoma, oligoastrocytoma and oligodendroglioma) and three tumor grades (WHO grades 2-4). Also, histopathological evaluation was performed by a pathologist on all the samples, yielding assessment of tumor cell concentration per sample, which was also an input into the modeling process.

4.4.2.2 Experiments and Results

We focus in this study on the mass spectrometry data between (*m/z*) 650-1000 Daltons, since we are focused on understanding and using the relationship of the lipid profile to all characteristics of gliomas (including grades, subtypes and tumor cell concentration). We perform peak selection using two techniques: t-statistics and KS-statistics. We bin the tumor cell concentration into three categories ($0-35\%$, $35-70\%$ and $70-100\%$) and use these categories to divide the available data into subgroups over which we compute the statistics. We then sort the statistics and select the masses with the highest(lowest) t-statistics (KS-statistics) as peaks to regress over. We conduct experiments to compare the performance of the two peak selection approaches, as well as the number of peaks used. We also explore via our test cases the effect of preliminary normalization on the mass spectrometry data.

We present our results from the comparison of preprocessing schemes in Table 4.4.2.2. We compare four schemes against the original data - scaling to lie in the $(0,1)$ range, scaling by the mean and standard deviation, scaling by the minimum and standard deviation, and preliminary baseline correction using a moving average. Figure 26 shows a visual comparison of these preprocessing schemes with the original data, for three sample spectra

chosen to represent three different tumor cell concentration levels ($5\%, 40\%, 90\%$). Table 4.4.2.2 shows the corresponding quantitative comparison of these schemes, with the modeling and prediction errors that were obtained for the respective schemes while using a sigmoid kernel-based RVM for modeling with 4 peaks selected using t-statistics. From extensive experiments over both peak selection methods and over different numbers of peaks, we observe that the preprocessing scheme that yields the best performance for this data set is the one where we scale the data by standard deviation and force the minimum to zero.

Finally, we conducted experiments to ascertain the optimal number of peaks to employ in this framework and these results are presented in Table 4.4.2.2. We compare a wide range of values for the number of peaks with both peak selection approaches. In looking at the modeling and prediction errors, we find that for this data set, 4 and 5 are the optimal number of peaks for the t-statistics-based and KS-statistics- based approaches respectively. Using a leave-N-out approach, we train the model on 80% of the available data set and test it on the remaining 20%. The errors from the respective sets are designated here as the modeling and prediction errors respectively, with these numbers being estimated as the average over a 100 independent trials. It is worth noting that while it can be expected that increasing the number of peaks would increase accuracy in the model by allowing more degrees of freedom, in our study, we observed diminishing returns when increasing the number of peaks beyond the optimal described above. We attribute this to the limited size of the population that we use for training the model, and we expect that increasing the number of samples analyzed will lead to higher accuracy (and allow this for a greater number of peaks).

4.4.3 Concluding remarks on tumor boundary detection

In this section, we proposed a novel method for intraoperative prediction of tumor cell concentration from MSI, based on a Relevance Vector Machine approach to be used in conjunction with appropriate peak selection methods for dimensionality reduction. The

Table 9: Comparison of preprocessing schemes: modeling and prediction errors using the sigmoid kernel for modeling, with t-statistics-based selection of 4 peaks

Preprocessing scheme	Modeling Error (%)	Prediction Error(%)
None *Original data*	25.80	25.72
Scaling (to lie in [0,1])	24.22	23.95
Scaling (by mean and standard deviation)	25.21	25.31
Scaling (by standard deviation) and minimum zero	13.21	14.59
Baseline correction (by moving average)	22.66	25.48

90mm

Table 10: Quantifying the model performance: comparing different peak selection methods and the number of peaks used

Peak selection method	Number of peaks	Modeling error (%)	Prediction error (%)
T-statistics	50	25.86	25.66
T-statistics	20	25.78	25.82
T-statistics	10	20.40	20.28
T-statistics	6	18.75	18.84
T-statistics	5	17.34	17.71
T-statistics	**4**	**13.21**	**14.59**
T-statistics	3	19.31	21.45
KS-statistics	50	25.74	25.94
KS-statistics	20	14.05	14.72
KS-statistics	10	13.37	14.22
KS-statistics	6	13.38	14.13
KS-statistics	**5**	**13.31**	**14.02**
KS-statistics	4	13.36	14.31
KS-statistics	3	14.07	15.01

prediction of tumor cell concentration, given a previously unseen spectrum acquired by the DESI-MS modality, was found to be achievable in real-time which makes an excellent case towards integrating the framework with the surgical workflow.

The framework yields promising results with a reasonably low error of 14% as tested by a leave-N-out approach to quantifying the prediction capability of the *learned* model. These results are especially promising given the limited size of the population we regress over in training the RVM. This also motivates our first goal for future work on this front, which is to increase the robustness of the modeling results and identify more suitable peaks by including a larger population of mass spectra into the analysis. We will also explore alternate peak selection and preprocessing techniques. We will especially pursue approaches to increase the model accuracy and its prediction capability by reducing inter-subject, inter-subtype and inter-grade variance. We aim to develop appropriate techniques for normalization of mass spectra towards this goal. Finally, we will address the issues of tumor density (as different from tumor cell concentration which is used in this work) and spatial interpolation, towards enabling the intraoperative use of the proposed framework for tumor boundary location.

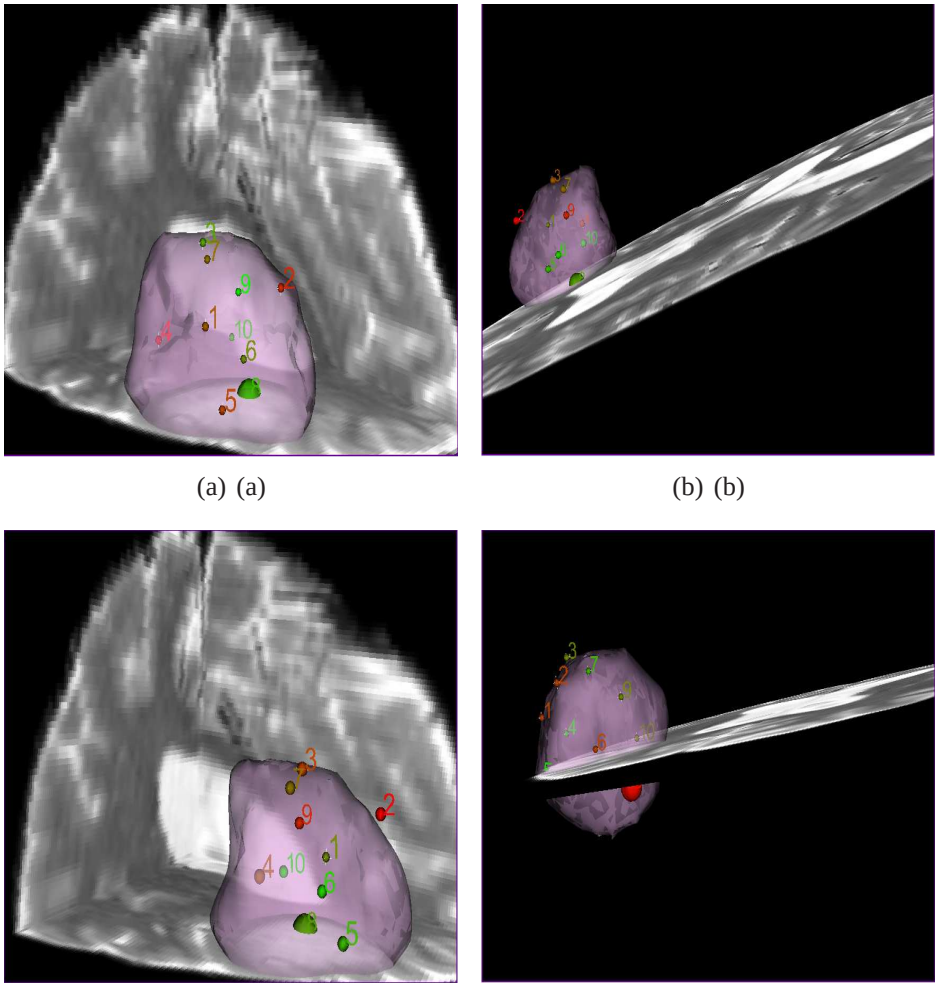

(a) (a) (b) (b)

(c) (c) (d) (d)

Figure 20: Visualization in Slicer3 of MS image data with respect to peaks selected by T-statistics (a,b,c for 768.3, 838.3 and 889.2 Dalton respectively) and tumor cell concentration (d), superimposed on the stereotactic sampling sites from the original tumor

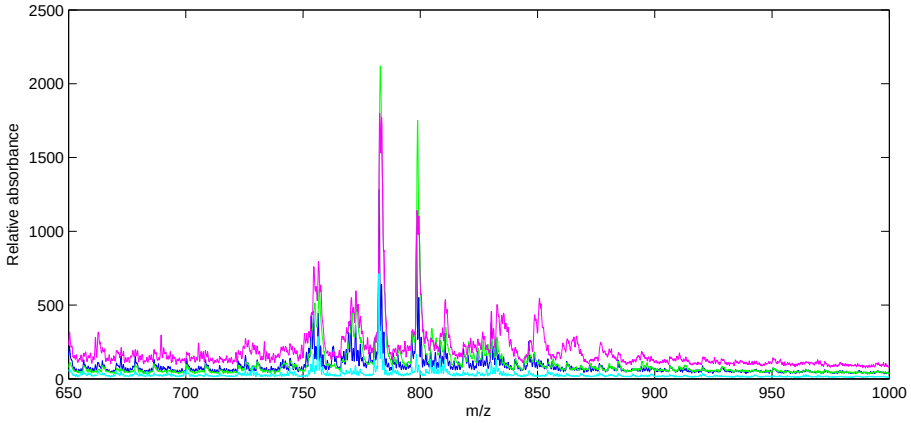

Figure 21: Visualization of sample mass spectra from the four glioma subtypes in the analysed dataset: anaplastic astrocytoma (blue), glioblastoma (green), oligodendroglioma (maroon) and oligoastrocytoma (cyan). The m/z range of 650-1000 is displayed.

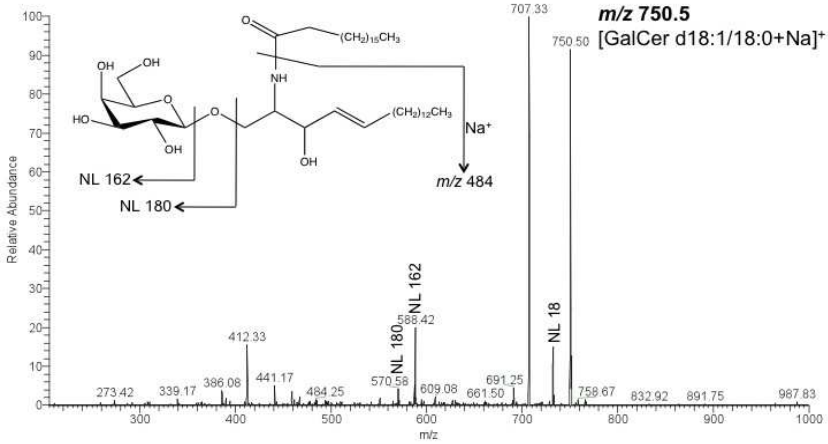

Figure 22: Tandem mass spectrum of m/z 750.5, assigned as the positively charged sodium adduct of GalCer(d18:1/18:0). Neutral loss (NL) of 162, forming m/z 588.4, and NL of 180, forming m/z 570.3, are both highly characteristic patterns in the first-generation product ion spectra for precursor ions of galactoceramides. A characteristic NL 18, corresponding to the loss of water is also observed. The fragment peak m/z 484.3 corresponds to the sodiated C18 sphingosine long-chain base, and represents a significant mass fragment ion for galactoceramides ([28]).

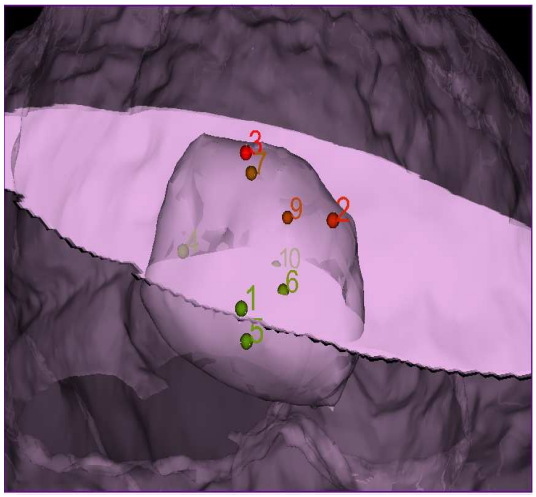

Figure 23: Visualization of stereotactic sampling sites on tumor surface for 1 subject

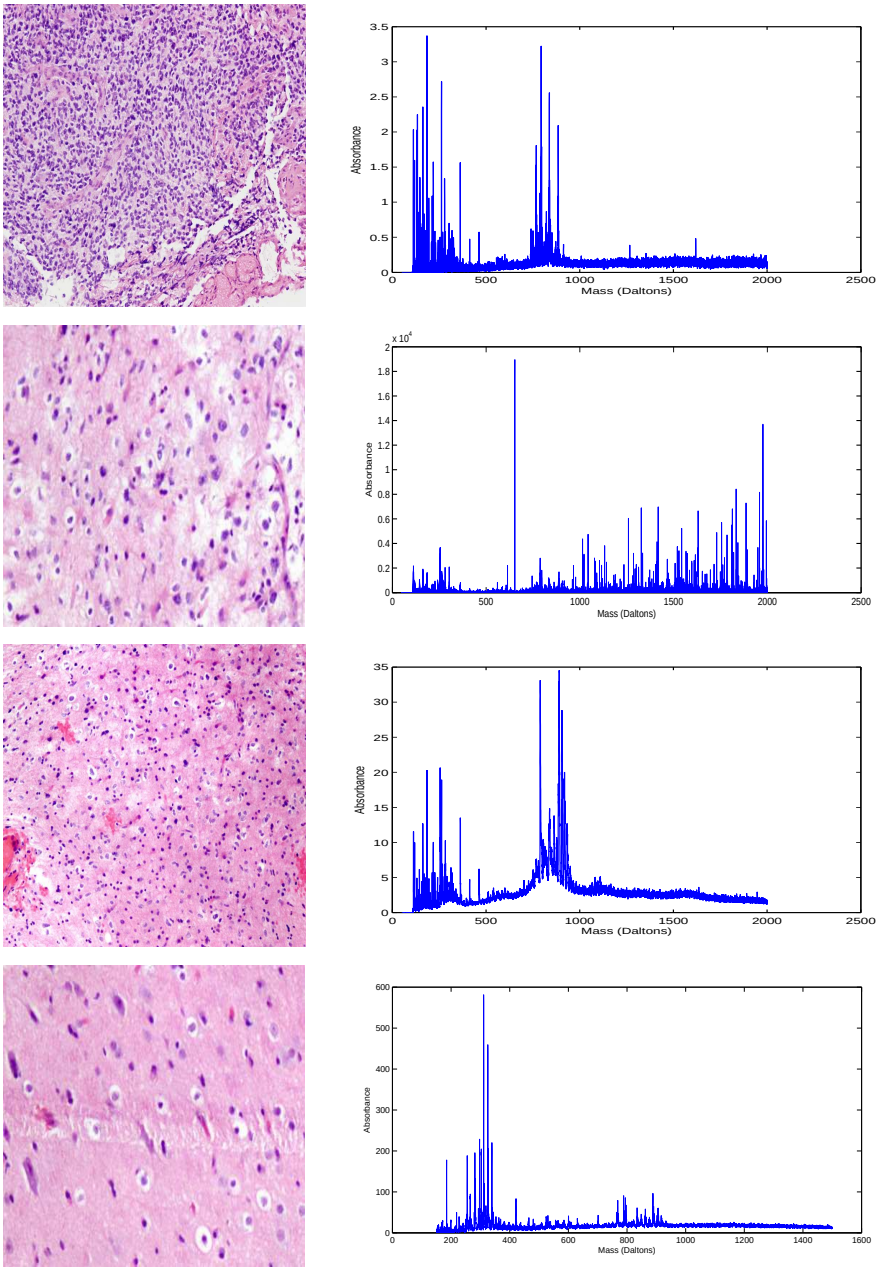

Figure 24: Sample tissue section stained with hematoxylin and eosin (H&E)s (left) and corresponding Profile Spectra (right): each row corresponds to one tumor cell concentration of 90%, 50%, 30% and 0-5% (top to bottom)

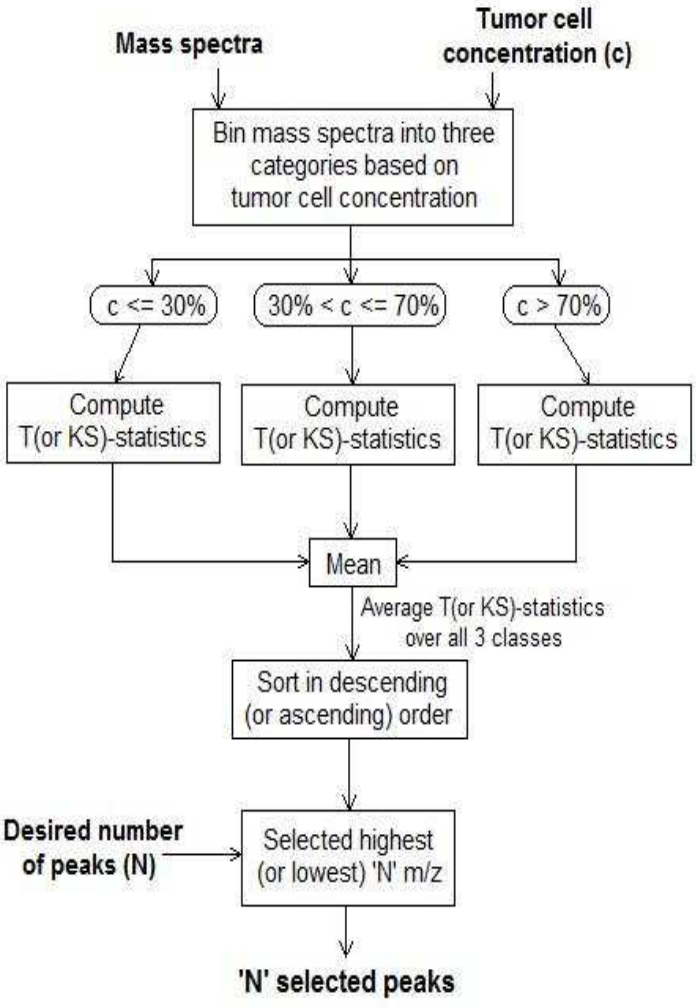

Figure 25: Flowchart for peak selection

Figure 26: Visual comparison of preprocessing schemes: sample spectra with tumor cell concentrations of 5%(red), 40%(green) and 95% (blue)

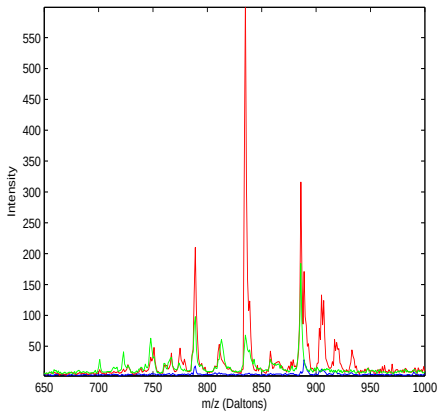

(a) Original spectra

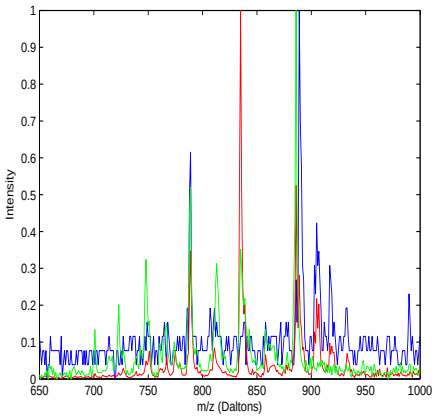

(b) Scaling to lie in $(0, 1)$

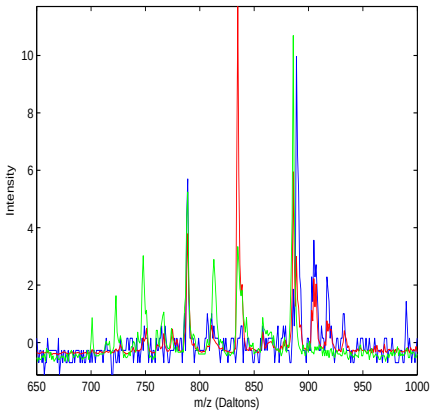

(c) Scaling by mean and standard deviation

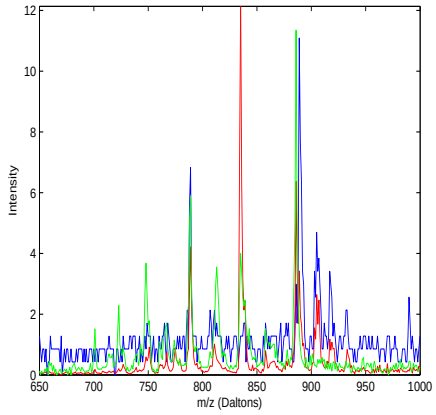

(d) Scaling by standard deviation, with 0 minimum

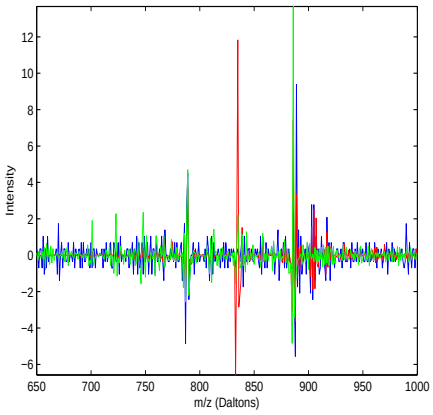

(e) Basic baseline correction (using moving averages)

CHAPTER V

CONCLUDING REMARKS

This thesis addresses the three research areas of the segmentation of neural fiber bundles and blood vessels, schizophrenia detection and finally the analysis of mass spectrometry imaging towards enabling its use as a medical imaging modality. While the work in this thesis puts forth new mathematical methods in each of these areas, they each hold further open research problems of great interest and practical application in the field of medical imaging.

The segmentation of neural fiber bundles and blood vessels are fields that have spurred a tremendous amount of research, but open issues abound with regard to the usability of the segmentation frameworks towards specific end-applications such as group studies in disorders such as schizophrenia and Alzheimer's disease, as well as quantification in cardiac disorders such as in plaque detection and evaluation.

Schizophrenia detection is a field that is still largely based on qualitative evaluation and hence still prone to misdiagnosis. Therefore, it is of vital importance to develop quantitative methods for robust schizophrenia detection. Due to the complexity of the disorder and the gaps in the understanding of the same from both anatomical and functional perspectives, it is important to both develop methods that aid in the detection of the disorder and methods that aid clinicians in expanding their understanding of the disorder. Methods that serve to understand white matter structures in a focused and individual manner (such as the framework of Chapter 3) are a useful contribution in the latter direction. It is of further interest to use different such frameworks in conjunction and understand their relative capabilities towards interpreting the results or *d*iagnosis from the different frameworks appropriately.

For example, while the proposed framework yields no classification between normal control and schizophrenic brains (with regard to the Cingulum Bundle) on the larger extended population, it does allow a comparison of the spatial variation in features between these classes. Coupled with the observation that the tubular surface segmentation framework extracts the tubular structure passing through the high FA voxels, the proposed framework can be used with alternate tractography algorithms to extract entire lengths of white matter bundles and subsequently capture a greater cross-section to allow voxels with lower FA (and hence lower directivity), which can be expected to yield better classification (and with greater generalization). Also, as mentioned earlier, the study of other white matter bundles (using the proposed and competing frameworks) is another area with great potential remaining to be studied.

Finally, mass spectrometry imaging analysis is a relatively new entrant in the field of medical imaging, and specifically the surgical use of the modality targeted by the work in this thesis is a very novel end-application of this modality. Coupled with the access to new enabling techniques such as DESI, the mathematical techniques proposed here for classification, biomarker detection and tumor boundary location are of vital significance. There are still open issues though with regard to the actual use of mass spectrometry in the surgical workflow and a great number of these stem from two fronts. The first is the paucity of mass spectrometry data to train quantitative frameworks on, and the associated impact of the specific natures and volume of data that certain mathematical techniques require, such as the need for the RVM-based regression framework to be trained on a population that is not only larger overall but also includes several samples from each subject, and contains ground truth (or expert markings) for tumor boundaries for enough of these subjects that the results can be quantitatively verified. The second set of issues stems from the lack of understanding around the nature of mass spectrometry data from a signal processing perspective. Greater understanding of the role of the subject (individual anatomy), the tumor type, the tumor grade, tumor cell density and so on will enable more accurate and

physiologically-motivated filtering and preprocessing techniques for MSI analysis which will greatly enhance the usability of all classification and modeling techniques for this modality of data.

APPENDIX A

DERIVATION OF TUBULAR SURFACE EVOLUTION

A.1 Derivation of Tubular Surface Evolution

In this section, we provide the detailed derivation of the evolutions equations for the proposed Tubular Surface model.

A.1.1 Sobolev Gradient in terms of the $\mathbb{L}^2$ Gradient

We begin by expressing the Sobolev gradient as a function of the standard $\mathbb{L}^2$ gradient, which can be using standard variational calculus. Let $\Gamma : [0,1] \to \mathbb{R}^d$ ($d = 3$ or $d = 4$) define a space curve such that $\Gamma(0) = \Gamma_0$ and $\Gamma(1) = \Gamma_1$ where $\Gamma_0, \Gamma_1 \in \mathbb{R}^d$ are the fixed endpoints of Γ. Let E be an energy defined on Γ, and let $g = \nabla_{Sob} E$, $f = \nabla_{\mathbb{L}^2} E$ denote the Sobolev and $\mathbb{L}^2$ gradients of E, respectively.

By the definition of the inner products (4) and (5), g and f are related as follows:

$$-L^2 g_{ss} = f, \quad g(0) = g(L) = 0 \tag{44}$$

where s represents the arclength parameter of Γ, L is the length of Γ, and the boundary condition corresponds to endpoints that are to be fixed during evolution. Equation 44 can be solved for g by integrating yielding:

$$g'(s) = g'(0) - \frac{1}{L^2} \int_0^s f(\hat{s})\, \mathrm{d}\hat{s}, \tag{45}$$

integrating again yields

$$\begin{aligned} g(s) &= g(0) + s g'(0) - \frac{1}{L^2} \int_0^s \int_0^{\hat{s}} f(\epsilon)\, \mathrm{d}\epsilon\, \mathrm{d}\hat{s} \\ &= s g'(0) - \frac{1}{L^2} \int_0^s f(\hat{s})(s - \hat{s})\, \mathrm{d}\hat{s} \end{aligned} \tag{46}$$

where

$$g'(0) = \frac{1}{L^3} \int_0^L f(\hat{s})(L - \hat{s})\, \mathrm{d}\hat{s}. \tag{47}$$

The expressions (46) and (45) above yield a linear complexity (in the number of sample points of Γ) computational algorithm for computing g in terms of f.

Since the transformation mapping f to g is a bounded linear operator, it can be expressed as an integral operator, i.e.,

$$g(s) = \int_0^L K(s, \hat{s}) f(\hat{s})\, \mathrm{d}\hat{s} =: K(f)(s), \tag{48}$$

where $s, \hat{s}$ are arclength parameters of Γ, $K : [0, L]^2 \to \mathbb{R}$ is a symmetric kernel, and by abuse of notation, we also write $g = K(f)$ to denote the linear operator defined above. By manipulation of (46) and (45), one can find that K is given as in (8). Note also that

$$g'(s) = \int_0^L \partial_s K(s, \hat{s}) f(\hat{s})\, \mathrm{d}\hat{s} =: (\partial_s K)(f)(s). \tag{49}$$

The expressions (48) and (49) are for simplicity of notation and ease of mathematical manipulation in the subsequent computations. However, for numerical implementation the expressions (48) and (49) are computed using the expressions (46) and (45), as doing so results in lower computational complexity.

A.1.2 Sobolev Gradient of Tubular Energy

We begin by computing the $\mathbb{L}^2$ gradient of the tubular energy (3). Let $\tilde{c} : [0, 1] \to \mathbb{R}^4$ and $\tilde{c} = (c, r)$ where $c : [0, 1] \to \mathbb{R}^3$ is immersed and $r : [0, 1] \to \mathbb{R}^+$. Denote by s in this subsection, the arclength parameter of c, by $\tilde{s}$ the arclength parameter of $\tilde{c}$, and by $u \in [0, 1]$ a parameter of a parameterization of $\tilde{c}$. Then (3) can we written

$$E(\tilde{c}) = \int_0^1 \Psi(\tilde{c}(u), \frac{c'(u)}{|c'(u)|}) |\tilde{c}'(u)|\, \mathrm{d}u,$$

where Ψ is a function of $p = (x, r) \in \mathbb{R}^4$ and $v \in \mathbb{S}^2$, $\tilde{s}$ is arclength parameter of the curve $\tilde{c}$. Letting $\tilde{c}$ be time-varying, we can compute the variation of E:

$$\frac{\mathrm{d}}{\mathrm{d}t}E = \int_0^1 \left(\Psi_p \cdot \tilde{c}_t + \Psi_v \cdot \frac{\mathrm{d}}{\mathrm{d}t}\frac{c'(u)}{|c'(u)|} \right) |\tilde{c}_u| + (\Psi \tilde{c}_{t\tilde{s}} \cdot \tilde{c}_{\tilde{s}} |\tilde{c}_u|) \, \mathrm{d}u,$$

which simplifies to

$$\frac{\mathrm{d}}{\mathrm{d}t}E = \int_0^1 \tilde{c}_t \cdot \left[\Psi_p - \frac{\partial}{\partial \tilde{s}} \left(\hat{\Psi}_v \sqrt{1 + \left(\frac{r_{\tilde{s}}}{|c_{\tilde{s}}|} \right)^2} + \Psi \tilde{c}_{\tilde{s}} \right) \right] \mathrm{d}\tilde{s}.$$

where $\hat{\Psi}_v = (\Psi_v, 0)^T$. Therefore,

$$\frac{1}{L}\nabla_{\mathbb{L}^2} E(\tilde{c}) = \Psi_p - \frac{\partial}{\partial \tilde{s}} \left(\hat{\Psi}_v \sqrt{1 + \left(\frac{r_{\tilde{s}}}{|c_{\tilde{s}}|} \right)^2} + \Psi \tilde{c}_{\tilde{s}} \right). \tag{50}$$

The Sobolev gradient is then computed using (48) and (50) yielding:

$$\begin{aligned} \nabla_{Sob} E &= K(\nabla_{\mathbb{L}^2} E) \\ &= L \cdot K(\Psi_p) + L \cdot \partial_{\hat{s}} K(\hat{\Psi}_v \sqrt{1 + (r_{\tilde{s}}/|c_{\tilde{s}}|)^2} + \Psi \tilde{c}_{\tilde{s}}) \end{aligned} \tag{51}$$

where the expressions for the operators $K()$ and $\partial_{\hat{s}} K()$ are given in (48) and (49), and they can be computed using formulas (46), (45), and (47).

APPENDIX B

FINSLER LEVELSETS FOR IMAGE SEGMENTATION IN ORIENTED DOMAINS

B.1 Motivation

This work was motivated by the problem of segmenting structures from imagery in oriented domains. Diffusion-Weighted Magnetic Resonance Imaging (DW-MRI or DWI) is a natural application scenario for this framework, but we also formulate the problem of textural segmentation as one of segmentation in an oriented domain (by extracting features that create an oriented domain) and subsequently demonstrate the use of the proposed framework for these two application scenarios.

For image data in oriented domains, the boundaries of objects of interest extremize energy functionals that depend not only on position but also on direction. This is the fundamental motivation behind the Finsler active contour framework since it attempts to extremize an energy of exactly this form. Prior work has implemented the dynamic programming based approach to this framework [61]. The work here presents the first level set implementation of this framework in arbitrary dimension and the results obtained with this implementation for 2D and 3D images. This implementation has the natural advantages of being able to handle topological changes, and being able to trivially extend our implementation to arbitrary dimension.

B.2 Theory and math

Let $\Psi(p, d)$ denote the energy that we desire to minimize as a function of the position 'p' and the direction 'd' . The expression for the evolution of the hypersurface is obtained as,

$$\Sigma_t = -\nabla_p \Psi . N + Tr(\nabla_{dd} \Psi) + \Psi . Tr(dN) N, \tag{52}$$

where Σ denotes the hypersurface, Ψ is the local cost, N denotes the unit normal to the hypersurface and dN is the shape operator. The detailed derivation of this expression can be found in [61].

Denoting the surface of interest as the zero level set of a signed distance function, we obtain the expression for the evolution of the level set function as,

$$u_t = \nabla_p \Psi . \nabla u + Tr(\nabla_{dd} \Psi) + \Psi . Tr(dN) ||u||, \tag{53}$$

where u is the level set function.

B.3 Level Set Implementation

The level set formulation implicitly represents the surface of interest as the zero level set of an appropriately dened level set function. This work uses the signed distance function because of its desirable properties with regards to the computation of geometrical quantities of interest in surface evolution. This choice simplies the computation of the Shape operator, dN , and a basis for the tangent space (which is equivalent to the surface derivatives with respect to the arc length parameter *s*).

B.3.1 Shape operator

Let u denote the signed distance function (SDF). Then, the normal can be obtained from the gradient of the SDF as,

$$N = \frac{\nabla u}{||\nabla u||} \tag{54}$$

Since the shape operator is the derivative of the normal to the surface with respect to arc length, s, we can write it as,

$$\frac{dN}{ds} = \frac{d}{ds} \frac{\nabla u}{||\nabla u||} \tag{55}$$

This can be simplied to obtain an expression for the shape operator in terms of the SDF as

$$dN = \frac{1}{||\nabla u||}(1 - N.N^t)H_u \tag{56}$$

where Hu is the pointwise hessian of the levelset function u.

B.3.2 Computation of surface derivatives

It can be seen that that with arc length parameterization and the fact that the surface derivatives required in the numeric implementation occur under a trace operator (which is invariant under a change of basis of the matrix argument or a change of order of argu- ments), we can replace the matrix containing surface derivatives by an arbitrary choice of basis for the tangent space at the point. This basis is trivial to determine if the unit normal to the surface is known. Since for an SDF, the normal can be obtained from the gradient, we can simply express the matrix with the tangent space basis as,

$$d\Sigma = (1 - N.N^t) \tag{57}$$

where $d\Sigma$ denotes the surface derivatives used in the evolution, and N denotes the unit normal to the surface Σ. It can be shown that the eigenvectors of this matrix are in fact the normal itself - corre- sponding to zero eigenvalue - and the (n-1) tangent directions corresponding to eigenvalue 1 which represent surface derivatives. The sparse eld approach of [94] was chosen to implement the level set formulation of the Finsler active contour framework, in order to achieve fast computations given the large sizes of the directional datasets being used.

B.3.3 Cost functions

The fundamental motivation to all the cost functions explored in this work is to nd edges in the directionality of the underlying data. Hence all the cost functions discussed here yield segmentations that are primarily edge-based in nature. A crucial feature of the available data is that the object of interest does not homogeneously display a single direction.

	Diffusion profile inside	Diffusion profile outside
Original data	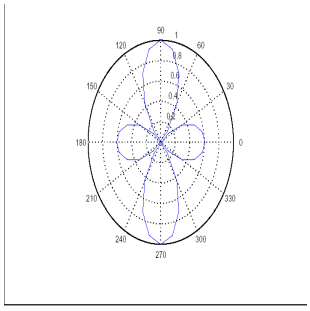	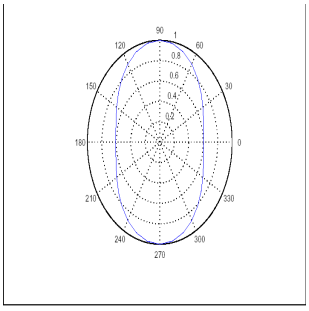
Tensor model approximation	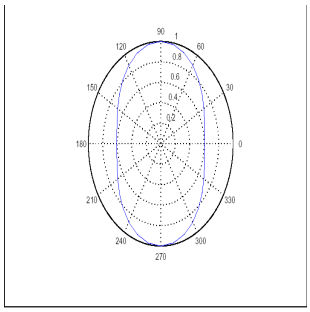	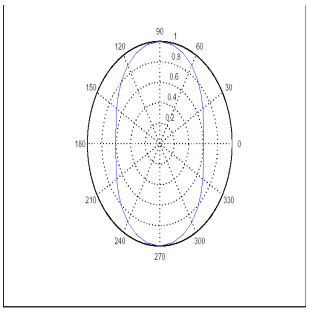

Table 11: Diffusion profiles in the synthetic image. Results of comparison in Figure 27

There are intermediate areas where (using DW-MRI terminology), the diffusion is possibly isotropic and sometimes zero. Thus, it is important to suitably compute gradients in these images to better capture the directionality inside (and outside) the evolving surface. The cost functions are formulated in such a way that the costs ranges from 0 to 1, and so that the energy is minimized on the surface of interest. The convergence condition was fairly simple with the algorithm stopping when the average cost on the surface fell below 0.1 and stayed there beyond a certain number of iterations.

B.4 Results

The framework was tested via three sets of experiments. The rst aimed to compare it with the Riemannian approach on a tensor t of the data. The second experiment applied the framework to the segmentation of a texture image and the third applied it towards automatically nding the cingulum bundle from DW-MRI imagery.

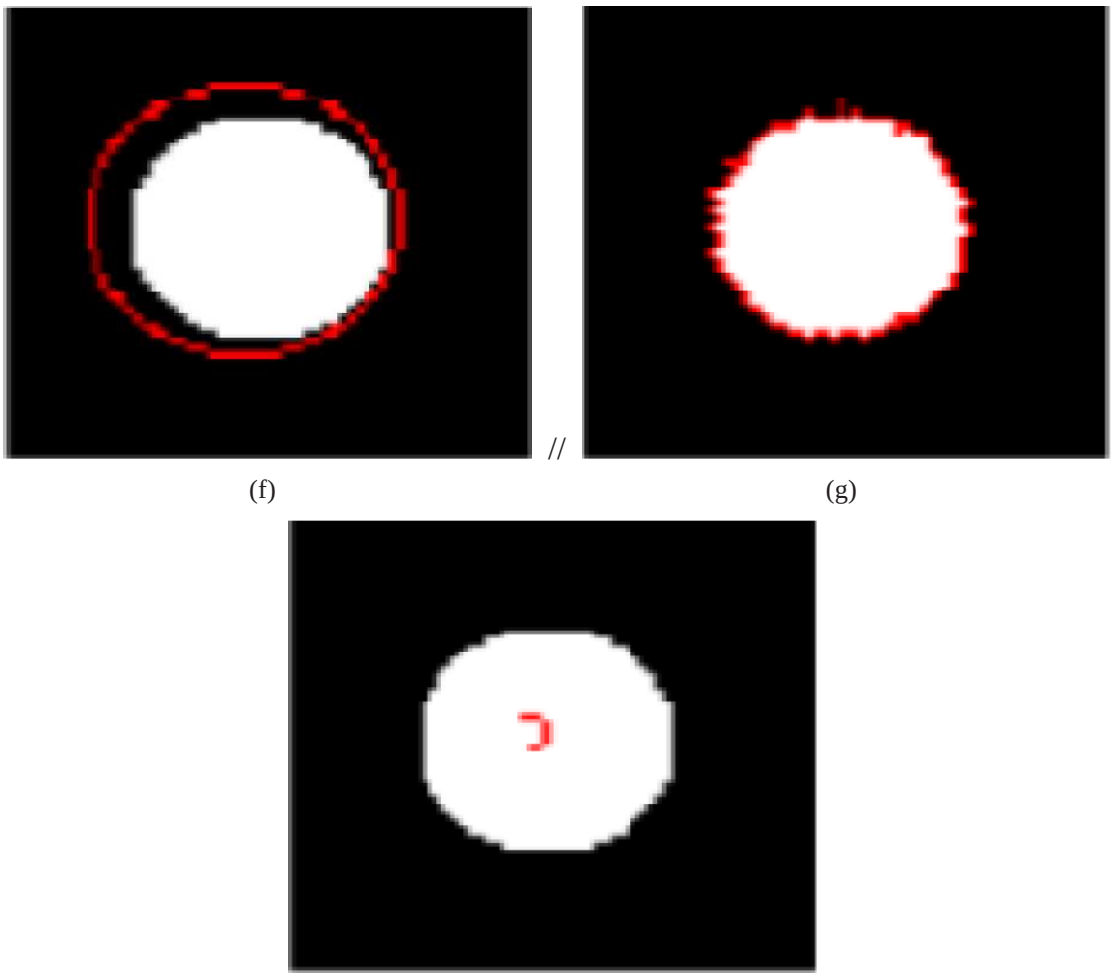

(f) // (g)

(h)

Figure 27: Results on synthetic data comparing Finsler-based framework to Riemannian approach using tensors. (a) shows the initial level set. (b) shows the result obtained using the Finsler level set framework, and (c) shows the result of applying Riemannian level sets on a tensor fit to the data. (Diffusion profiles are provided in Table 11).

B.4.1 Synthetic data

One of the advantages of the Finsler active contour framework is the fact that the data is not forced to t a tensor model. This allows greater accuracy in capturing features of interest. This is demonstrated via a comparison between the proposed framework and a Riemannian approach applied to a tensor approximation of the same data set (Figure 27). A synthetic data set was constructed with different diffusion proles within and outside the object of interest which is a simple circle. It is an extreme example since the diffusion proles within and outside the circle look identical when t to a tensor model (Table 11). This experiment though simplied, clearly illustrates the advantage of our framework.

B.4.2 Texture segmentation

For textural segmentation, the transformation of the available data into an oriented domain is crucial to the effectiveness of the proposed segmentation algorithm. This transformation is dependent upon the nature of the image that we desire to segment. In the images used in this work, it is of interest to separate the directionality of the gradients of the image inside and outside the object. Hence, the transformation that we employ to construct the feature data for this application is to compute the directional gradients of the given image. The gradients are comparable to the diffusion prole for DW-MRI imagery and the directions in which these gradients are computed are analogous to the sampling directions. Figure 28 illustrates this. Figure 29 shows a comparison of the method with the intensity edge-based approach, and clearly demonstrates the advantage we gain by adding directionality into the segmentation problem via the transformation into an oriented domain. It is observed that with a purely intensity edge-based approach, for this image, the segmentation process is not well-behaved and does not converge.

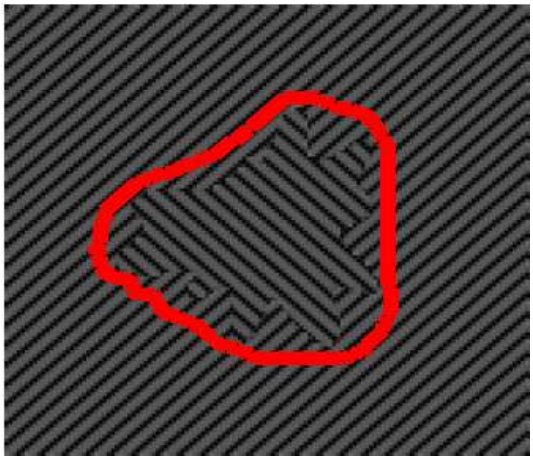

// vspace5mm

(a)

(b)

Figure 28: Result on texture image. (a) shows the initial levelset and (b) shows the (smoothed) result from the Finsler levelset framework.

(a)

(b)

Figure 29: Comparison between (a) intensity edge-based approach and (b) directional edge-based (proposed) approach for same initial level set.

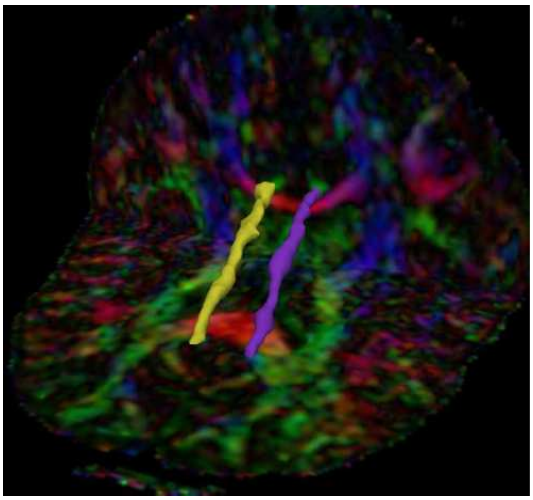

Figure 30: Result on DW-MRI data. The structures in yellow and magenta indicate the CB surface identified in the right and left hemisphere of the brain volume.

B.4.3 CB Segmentation from DWI data

The object of interest in the available DW-MRI imagery is the cingulum bundle. We can deduce the equivalence between such a dataset and the image on which the textural segmentation has been demonstrated. The stripes in the textural image are analogous to the bers within the cingulum bundle that we desire to encapsulate within a single surface. The same cost function was in fact applied to both these data sets with no difference other than the dimension of the data itself. The initial level set for this application was arrived at by creating the surface of smallest volume that fully contains the anchor tract that is obtained out of the Finsler tractography module discussed in [61]. In DW-MRI data, the task of segmenting the cingulum bundle is equivalent to nd disjoint bers in the available brain volume that are similarly aligned. In the absence of ground truth for the cingulum bundle in the available data, we use the availability of simple eigenvalue analysis based approximations to the cingulum bundle along with visual verication to validate the performance of the algorithm on the DW-MRI data. Based on these, the CB extracted is found to be satisfactory as shown in Figure 30.

B.5 Concluding remarks

The proposed framework gives us a method to automatically segment the cingulum bundle from the DW-MRI volume and the results were validated by comparison with eigen value based thresholding and visual inspection. Also, the texture segmentation examples shown in here were chosen because of their similarity to DW-MRI data in the sense of separating directionality inside and outside the object, and to demonstrate the advantage of adding directionality to the image segmentation framework.

REFERENCES

[1] *Control Theory and Fast Marching Techniques for Brain Connectivity Mapping*, 2006.

[2] AGAM, G. and WU, C., "Probabilistic modeling based vessel enhancement in thoracic CT scans," in *IEEE Computer Society Conference on Computer Vision and Pattern Recognition, 2005. CVPR 2005*, vol. 2, 2005.

[3] AGAR, N., MALCOLM, J., MOHAN, V., YANG, H., JOHNSON, M., TANNENBAUM, A., AGAR, J., and BLACK, P., "Imaging of Meningioma Progression by Matrix-Assisted Laser Desorption Ionization Time-of-Flight Mass Spectrometry," *Analytical Chemistry*, pp. 97–109.

[4] AWATE, S. P., 0005, H. Z., and GEE, J. C., "Fuzzy nonparametric dti segmentation for robust cingulum-tract extraction," in *MICCAI (1)* (AYACHE, N., OURSELIN, S., and MAEDER, A. J., eds.), vol. 4791 of *Lecture Notes in Computer Science*, pp. 294–301, Springer, 2007.

[5] BAIANO, M., DAVID, A., VERSACE, A., CHURCHILL, R., BALESTRIERI, M., and BRAMBILLA, P., "Anterior cingulate volumes in schizophrenia: a systematic review and a meta-analysis of MRI studies," *Schizophrenia research*, vol. 93, no. 1-3, pp. 1–12, 2007.

[6] BELJEBBAR, A., DUKIC, S., AMHARREF, N., BELLEFQIH, S., and MANFAIT, M., "Monitoring of Biochemical Changes through the C6 Gliomas Progression and Invasion by Fourier Transform Infrared (FTIR) Imaging," *Analytical Chemistry*, pp. 6962–6970.

[7] BENES, F., "Relationship of cingulate cortex to schizophrenia and other psychiatric disorders," *Neurobiology of Cingulate Cortex and Limbic Thalamus: A Comprehensive Handbook. Boston: Birkhäuser*, pp. 581–605, 1993.

[8] BINFORD, T., "Visual perception by computer," in *IEEE conference on Systems and Control*, vol. 261, 1971.

[9] BISHOP, C. and TIPPING, M., "Variational relevance vector machines," in *Proceedings of the 16th Conference on Uncertainty in Artificial Intelligence*, pp. 46–53, 2000.

[10] BOUIX, S., SIDDIQI, K., and TANNENBAUM, A., "Flux driven automatic centerline extraction," *Medical Image Analysis*, vol. 9, no. 3, pp. 209–221, 2005.

[11] CALDWELL, R. and CAPRIOLI, R., "Tissue profiling by mass spectrometry: a review of methodology and applications," *Molecular & Cellular Proteomics*, vol. 4, no. 4, p. 394, 2005.

[12] CAPRIHAN, A., PEARLSON, G., and CALHOUN, V., "Application of principal component analysis to distinguish patients with schizophrenia from healthy controls based on fractional anisotropy measurements," *Neuroimage*, vol. 42, no. 2, pp. 675–682, 2008.

[13] CHAN, T. and VESE, L., "Active contours without edges," *Image Processing, IEEE Transactions on*, vol. 10, no. 2, pp. 266–277, 2001.

[14] CHAURAND, P., SANDERS, M., JENSEN, R., and CAPRIOLI, R., "Proteomics in diagnostic pathology: profiling and imaging proteins directly in tissue sections," *American Journal of Pathology*, vol. 165, no. 4, p. 1057, 2004.

[15] CHAURAND, P., SCHWARTZ, S., BILLHEIMER, D., XU, B., CRECELIUS, A., and CAPRIOLI, R., "Integrating histology and imaging mass spectrometry," *Anal. Chem*, vol. 76, no. 4, pp. 1145–1155, 2004.

[16] CHRISTENSEN, G. E. and SONKA, M., eds., *Information Processing in Medical Imaging, 19th International Conference, IPMI 2005, Glenwood Springs, CO, USA, July 10-15, 2005, Proceedings*, vol. 3565 of *Lecture Notes in Computer Science*, Springer, 2005.

[17] COHEN, L. D. and KIMMEL, R., "Global minimum for active contour models: A minimal path approach," in *CVPR*, pp. 666–673, IEEE Computer Society, 1996.

[18] COHEN-ADAD, J., DESCOTEAUX, M., ROSSIGNOL, S., HOGE, R. D., DERICHE, R., and BENALI, H., "Detection of multiple pathways in the spinal cord white matter using q-ball imaging," in *IEEE International Symposium on Biomedical Imaging : From Nano to Macro*, 2008.

[19] CONTURO, T., LORI, N., CULL, T., AKBUDAK, E., SNYDER, A., SHIMONY, J., MCKINSTRY, R., BURTON, H., and RAICHLE, M., "Tracking neuronal fiber pathways in the living human brain," *Proc. Natl. Acad. Sci USA*, vol. 96, no. 18, pp. 10422–10427, 1999.

[20] COOKS, R., OUYANG, Z., TAKATS, Z., and WISEMAN, J., "Ambient mass spectrometry," 2006.

[21] COOMBES, K., TSAVACHIDIS, S., MORRIS, J., BAGGERLY, K., HUNG, M., and KUERER, H., "Improved peak detection and quantification of mass spectrometry data acquired from surface-enhanced laser desorption and ionization by denoising spectra with the undecimated discrete wavelet transform," *Proteomics*, vol. 5, no. 16, pp. 4107–4117, 2005.

[22] COROUGE, I., FLETCHER, P., JOSHI, S., GOUTTARD, S., and GERIG, G., "Fiber tract-oriented statistics for quantitative diffusion tensor MRI analysis," *Medical Image Analysis*, vol. 10, no. 5, pp. 786–798, 2006.

[23] CRAMMER, K. and SINGER, Y., "On the algorithmic implementation of multiclass kernel-based vector machines," *The Journal of Machine Learning Research*, vol. 2, pp. 265–292, 2002.

[24] CRISTIANINI, N. and SHAWE-TAYLOR, J., *An introduction to support Vector Machines: and other kernel-based learning methods*. Cambridge Univ Pr, 2000.

[25] DAVIS, K., STEWART, D., FRIEDMAN, J., BUCHSBAUM, M., HARVEY, P., HOF, P., BUXBAUM, J., and HAROUTUNIAN, V., "White Matter Changes in Schizophrenia Evidence for Myelin-Related Dysfunction," 2003.

[26] DEMUTH, H. and BEALE, M., *Neural Network Toolbox: for use with MATLAB*. The Math Works, 2001.

[27] DIAMANDIS, E., "Mass spectrometry as a diagnostic and a cancer biomarker discovery tool: opportunities and potential limitations," *Molecular & Cellular Proteomics*, vol. 3, no. 4, p. 367, 2004.

[28] EBERLIN, L., DILL, A., GOLBY, A., LIGON, K., WISEMAN, J., COOKS, R., and AGAR, N.Y, R., "Discrimination of Human Astrocytoma Subtypes by Lipid Analysis using Desorption Electrospray Ionization Imaging Mass Spectrometry," *Angewandte Chemie*, pp. 6962–6970.

[29] ECKSTEIN, I., SHATTUCK, D., STEIN, J., MCMAHON, K., DE ZUBICARAY, G., WRIGHT, M., THOMPSON, P., and TOGA, A., "Active fibers: Matching deformable tract templates to diffusion tensor images," *Neuroimage*, vol. 47, pp. 82–89, 2009.

[30] FLORIN, C., PARAGIOS, N., and WILLIAMS, J., "Particle filters, a quasi-Monte Carlo solution for segmentation of coronaries," *Medical Image Computing and Computer-Assisted Intervention–MICCAI 2005*, pp. 246–253.

[31] FRANGI, A., NIESSEN, W., HOOGEVEEN, R., VAN WALSUM, T., and VIERGEVER, M., "Model-based quantitation of 3-D magnetic resonance angiographic images," *IEEE Transactions on Medical Imaging*, vol. 18, no. 10, pp. 946–956, 1999.

[32] FRIMAN, O., FARNEBÄCK, G., and WESTIN, C.-F., "A bayesian approach for stochastic white matter tractography," *IEEE Trans. Med. Imaging*, vol. 25, no. 8, pp. 965–978, 2006.

[33] FRISTON, K., "The disconnection hypothesis," *Schizophrenia Research*, vol. 30, no. 2, pp. 115–125, 1998.

[34] FUJIWARA, H., NAMIKI, C., HIRAO, K., MIYATA, J., SHIMIZU, M., FUKUYAMA, H., SAWAMOTO, N., HAYASHI, T., and MURAI, T., "Anterior and posterior cingulum abnormalities and their association with psychopathology in schizophrenia: A diffusion tensor imaging study," *Schizophrenia Research*, vol. 95, no. 1-3, pp. 215–222, 2007.

[35] GERHARD, M., DEININGER, S., and SCHLEIF, F., "Statistical classification and visualization of MALDI-imaging data," in *Proceedings of the 20th IEEE Symposium on Computer-based Medical SystemsKokol P, Zorman M, Podgerelec V, et al, eds*, pp. 403–5, 2007.

[36] GOODLETT, C., FLETCHER, P., GILMORE, J., and GERIG, G., "Group analysis of DTI fiber tract statistics with application to neurodevelopment," *Neuroimage*, 2008.

[37] HAKAK, Y., WALKER, J., LI, C., WONG, W., DAVIS, K., BUXBAUM, J., HAROUTUNIAN, V., and FIENBERG, A., "Genome-wide expression analysis reveals dysregulation of myelination-related genes in chronic schizophrenia," *Proceedings of the National Academy of Sciences*, vol. 98, no. 8, p. 4746, 2001.

[38] HARTIGAN, J. and WONG, M., "A K-means clustering algorithm," *JR Stat. Soc. Ser. C-Appl. Stat*, vol. 28, pp. 100–108, 1979.

[39] HORN, B., *Robot vision*. MIT press, 1986.

[40] IFA, D., WISEMAN, J., SONG, Q., and COOKS, R., "Development of capabilities for imaging mass spectrometry under ambient conditions with desorption electrospray ionization (DESI)," *International Journal of Mass Spectrometry*, vol. 259, no. 1-3, pp. 8–15, 2007.

[41] KANUNGO, T., MOUNT, D., NETANYAHU, N., PIATKO, C., SILVERMAN, R., and WU, A., "An Efficient k-Means Clustering Algorithm: Analysis and Implementation," *IEEE Transactions on Pattern Analysis and Machine Intelligence*, pp. 881–892, 2002.

[42] KAY, S., FLSZBEIN, A., and OPFER, L., "The positive and negative syndrome scale (PANSS) for schizophrenia," *Schizophrenia bulletin*, vol. 13, pp. 261–276, 1987.

[43] KING, D., "dlib c++ library," March 2010. `http://dlib.net/`.

[44] KOHLER, M., MACHILL, S., SALZER, R., and KRAFFT, C., "Characterization of lipid extracts from brain tissue and tumors using Raman spectroscopy and mass spectrometry," *Analytical and Bioanalytical Chemistry*, vol. 393, no. 5, pp. 1513–1520, 2009.

[45] KUBICKI, M., WESTIN, C., NESTOR, P., WIBLE, C., FRUMIN, M., MAIER, S., KIKINIS, R., JOLESZ, F., MCCARLEY, R., and SHENTON, M., "Cingulate fasciculus integrity disruption in schizophrenia: a magnetic resonance diffusion tensor imaging study," *Biological Psychiatry*, vol. 54, no. 11, pp. 1171–1180, 2003.

[46] LENGLET, C., ROUSSON, M., and DERICHE, R., "Dti segmentation by statistical surface evolution," *IEEE Trans. Med. Imaging*, vol. 25, no. 6, pp. 685–700, 2006.

[47] LENGLET, C., ROUSSON, M., DERICHE, R., FAUGERAS, O. D., LEHERICY, S., and UGURBIL, K., "A riemannian approach to diffusion tensor images segmentation," in Christensen and Sonka [16], pp. 591–602.

[48] LESAGE, D., ANGELINI, E., BLOCH, I., and FUNKA-LEA, G., "A review of 3D vessel lumen segmentation techniques: Models, features and extraction schemes," *Medical Image Analysis*, 2009.

[49] LEVNER, I., "Feature selection and nearest centroid classification for protein mass spectrometry," *BMC bioinformatics*, vol. 6, no. 1, p. 68, 2005.

[50] LI, H. and YEZZI, A., "Vessels as 4-d curves: Global minimal 4-d paths to extract 3-d tubular surfaces and centerlines," *IEEE Transactions on Medical Imaging*, vol. 26, no. 9, pp. 1213–1223, 2007.

[51] LI, J., ZHANG, Z., ROSENZWEIG, J., WANG, Y., and CHAN, D., "Proteomics and bioinformatics approaches for identification of serum biomarkers to detect breast cancer," *Clinical Chemistry*, vol. 48, no. 8, p. 1296, 2002.

[52] LI, R. and OURSELIN, S., "Accurate Curvilinear Modelling for Precise Measurements of Tubular Structures," in *Digital Image Computing: Techniques and Applications; Proceedings of the VIIth Biennial Australian Pattern Recognition Society Conference, DICTA 2003*, p. 243, Citeseer, 2003.

[53] LIANG, X., ZHUANG, Q., CAO, N., and ZHANG, J., "Shape Modeling and Clustering of White Matter Fiber Tracts Using Fourier Descriptors," in *IEEE Symposium on Computational Intelligence in Bioinformatics and Computational Biology, 2009. CIBCB'09*, pp. 292–297, 2009.

[54] LIU, H., BONNER, A., and EMILI, A., "Modeling protein tandem mass spectrometry data with an extended linear regression strategy," in *Engineering in Medicine and Biology Society, 2004. IEMBS'04. 26th Annual International Conference of the IEEE*, vol. 2, 2004.

[55] LIU, J., RANKA, S., and KAHVECI, T., "Classification and feature selection algorithms for multi-class CGH data," *Bioinformatics*, vol. 24, no. 13, 2008.

[56] LORIGO, L. M., GRIMSON, W. E. L., FAUGERAS, O. D., KERIVEN, R., KIKINIS, R., NABAVI, A., and WESTIN, C.-F., "Codimension - two geodesic active contours for the segmentation of tubular structures," in *CVPR*, pp. 1444–1451, IEEE Computer Society, 2000.

[57] MADDAH, M., GRIMSON, W., WARFIELD, S., and WELLS, W., "A unified framework for clustering and quantitative analysis of white matter fiber tracts," *Medical image analysis*, vol. 12, no. 2, pp. 191–202, 2008.

[58] MADDAH, M., KUBICKI, M., WELLS, W., WESTIN, C., SHENTON, M., and GRIMSON, W., "Findings in schizophrenia by tract-oriented DT-MRI analysis," *Medical Image Computing and Computer-Assisted Intervention–MICCAI 2008*, pp. 917–924, 2008.

[59] MANNIESING, R. and NIESSEN, W., "Local speed functions in level set based vessel segmentation," *Medical Image Computing and Computer-Assisted Intervention–MICCAI 2004*, pp. 475–482.

[60] MANNIESING, R., VELTHUIS, B., VAN LEEUWEN, M., VAN DER SCHAAF, I., VAN LAAR, P., and NIESSEN, W., "Level set based cerebral vasculature segmentation and diameter quantification in ct angiography," *Medical Image Analysis*, 2006.

[61] MELONAKOS, J., PICHON, E., ANGENENT, S., and TANNENBAUM, A., "Finsler active contours," *IEEE Transactions on Pattern Analysis and Machine Intelligence*, 2008.

[62] MELONAKOS, J., MOHAN, V., NIETHAMMER, M., SMITH, K., KUBICKI, M., and TANNENBAUM, A., "Finsler tractography for white matter connectivity analysis of the cingulum bundle," in *MICCAI (1)*, pp. 36–43, 2007.

[63] MELONAKOS, J., NIETHAMMER, M., MOHAN, V., SMITH, K., KUBICKI, M., and TANNENBAUM, A., "Locally-constrained region-based methods for dw-mri segmentation," in *MMBIA*, 2007.

[64] MOHAN, V., SUNDARAMOORTHI, G., KUBICKI, M., TERRY, D., and TANNENBAUM, A., "Population analysis of the cingulum bundle using the tubular surface model for schizophrenia detection," in *SPIE Medical Imaging*, 2010.

[65] MOHAN, V., SUNDARAMOORTHI, G., STILLMAN, A., and TANNENBAUM, A., "Vessel Segmentation with Automatic Centerline Extraction Using Tubular Tree Segmentation," *MICCAI Cardiovascular Interventional Imaging and Biophysical Modelling Workshop 2009*, Under review.

[66] MONTAGNAT, J., "Deformable Modelling for 3D and 4D Medical Image Segmentation.," 1999.

[67] MORI, S., CRAIN, B., CHACKO, V., and VAN ZIJL, P., "Three dimensional tracking of axonal projections in the brain by magnetic resonance imaging," *Ann. of Neurol.*, vol. 45, no. 2, pp. 265–269, 1999.

[68] NAIN, D., YEZZI, A. J., and TURK, G., "Vessel segmentation using a shape driven flow," in *MICCAI (1)* (BARILLOT, C., HAYNOR, D. R., and HELLIER, P., eds.), vol. 3216 of *Lecture Notes in Computer Science*, pp. 51–59, Springer, 2004.

[69] NORRIS, J., CORNETT, D., MOBLEY, J., ANDERSSON, M., SEELEY, E., CHAURAND, P., and CAPRIOLI, R., "Processing MALDI mass spectra to improve mass spectral direct tissue analysis," *International journal of mass spectrometry*, vol. 260, no. 2-3, pp. 212–221, 2007.

[70] O'DONNELL, T., BOULT, T., FANG, X., and GUPTA, A., "The extruded generalized cylinder: a deformable model for objectrecovery," in *1994 IEEE Computer Society Conference on Computer Vision and Pattern Recognition, 1994. Proceedings CVPR'94.*, pp. 174–181, 1994.

[71] O'DONNELL, T., DUBUISSON-JOLLY, M., and GUPTA, A., "A Cooperative Framework for Segmentation using Contours and 3D Hybrid Models as Applied to Branching Cylindrical Structures," in *Proceedings of the Sixth International Conference on Computer Vision*, p. 454, IEEE Computer Society, 1998.

[72] PARK, H., WESTIN, C., KUBICKI, M., MAIER, S., NIZNIKIEWICZ, M., BAER, A., FRUMIN, M., KIKINIS, R., JOLESZ, F., MCCARLEY, R., and OTHERS, "White matter hemisphere asymmetries in healthy subjects and in schizophrenia: a diffusion tensor MRI study," *Neuroimage*, vol. 23, no. 1, pp. 213–223, 2004.

[73] PARKER, G. J. M., WHEELER-KINGSHOTT, C. A. M., and BARKER, G. J., "Estimating distributed anatomical brain connectivity using fast marching methods and diffusion tensor imaging," *IEEE Trans. Med. Imaging*, vol. 21, no. 5, pp. 505–512, 2002.

[74] PERRIN, M., POUPON, C., COINTEPAS, Y., RIEUL, B., GOLESTANI, N., PALLIER, C., RIVIÈRE, D., CONSTANTINESCO, A., BIHAN, D. L., and MANGIN, J.-F., "Fiber tracking in q-ball fields using regularized particle trajectories," in Christensen and Sonka [16], pp. 52–63.

[75] PICHON, E., "Novel methods for multidimensional image segmentation," 2005.

[76] PICHON, E., WESTIN, C.-F., and TANNENBAUM, A., "Anisotropic conformal flows and dt-mri tractography," in *MICCAI*, 2005.

[77] SCHAAP, M., METZ, C., VAN WALSUM, T., VAN DER GIESSEN, A., WEUSTINK, A., MOLLET, N., BAUER, C., BOGUNOVIĆ, H., CASTRO, C., DENG, X., and OTHERS, "Standardized evaluation methodology and reference database for evaluating coronary artery centerline extraction algorithms," *Medical Image Analysis*, vol. 13, no. 5, pp. 701–714, 2009.

[78] SCHMAHMANN, J. and PANDYA, D., *Fiber Pathways of the Brain*. Oxford University Press, 2006.

[79] SKELLY, L., CALHOUN, V., MEDA, S., KIM, J., MATHALON, D., and PEARLSON, G., "Diffusion tensor imaging in schizophrenia: Relationship to symptoms," *Schizophrenia Research*, 2008.

[80] SKOLD, M., RYDEN, T., SAMUELSSON, V., BRATT, C., EKBLAD, L., OLSSON, H., and BALDETORP, B., "Regression analysis and modelling of data acquisition for SELDI-TOF mass spectrometry," *Bioinformatics*, vol. 23, no. 11, p. 1401, 2007.

[81] SMIRNIOTOPOULOS, J., "The new WHO classification of brain tumors.," *Neuroimaging Clinics of North America*, vol. 9, no. 4, p. 595, 1999.

[82] SUNDARAMOORTHI, G., YEZZI, A. J., MENNUCCI, A., and SAPIRO, G., "New possibilities with Sobolev active contours," in *SSVM*, pp. 153–164, 2007.

[83] TAKASE, K., TAMAGAKI, C., OKUGAWA, G., NOBUHARA, K., MINAMI, T., SUGIMOTO, T., SAWADA, S., and KINOSHITA, T., "Reduced white matter volume of the caudate nucleus in patients with schizophrenia," *Neuropsychobiology*, vol. 50, no. 4, pp. 296–300, 2004.

[84] TAKATS, Z., WISEMAN, J., GOLOGAN, B., and COOKS, R., "Mass spectrometry sampling under ambient conditions with desorption electrospray ionization," 2004.

[85] TIBSHIRANI, R., HASTIE, T., NARASIMHAN, B., SOLTYS, S., SHI, G., KOONG, A., and LE, Q., "Sample classification from protein mass spectrometry, by peak probability contrasts," *Bioinformatics*, vol. 20, no. 17, p. 3034, 2004.

[86] TIPPING, M., "Relevance vector machine," Oct. 14 2003. US Patent 6,633,857.

[87] VAN BEMMEL, C., WINK, O., VERDONCK, B., VIERGEVER, M., and NIESSEN, W., "Blood pool contrast-enhanced MRA: improved arterial visualization in the steady state," *IEEE transactions on medical imaging*, vol. 22, no. 5, pp. 645–652, 2003.

[88] VASILEVSKIY, A. and SIDDIQI, K., "Flux maximizing geometric flows," *IEEE Trans. Pattern Anal. Mach. Intell.*, vol. 24, no. 12, pp. 1565–1578, 2002.

[89] WAGNER, M., NAIK, D., and POTHEN, A., "Protocols for disease classification from mass spectrometry data," *PROTEOMICS-Clinical Applications*, vol. 3, no. 9, pp. 1692–1698.

[90] WANG, F., SUN, Z., CUI, L., DU, X., WANG, X., ZHANG, H., CONG, Z., HONG, N., and ZHANG, D., "Anterior cingulum abnormalities in male patients with schizophrenia determined through diffusion tensor imaging," 2004.

[91] WANG, L. and BHALERAO, A., "Model Based Detection of Branching Structures," *Proc. Medical Image Understanding and Analysis, Portsmouth, UK*, 2002.

[92] WANG, Z. and VEMURI, B. C., "Dti segmentation using an information theoretic tensor dissimilarity measure," *IEEE Trans. Med. Imaging*, vol. 24, no. 10, pp. 1267–1277, 2005.

[93] WEN, P. and KESARI, S., "Malignant gliomas in adults," *New England Journal of Medicine*, vol. 359, no. 5, p. 492, 2008.

[94] WHITAKER, R., "A level-set approach to 3D reconstruction from range data," *International Journal of Computer Vision*, vol. 29, no. 3, p. 231, 1998.

[95] WILSON, D., NOBLE, J., and CSIRO, N., "An adaptive segmentation algorithm for time-of-flight MRA data," *IEEE transactions on medical imaging*, vol. 18, no. 10, pp. 938–945, 1999.

[96] WISEMAN, J., PUOLITAIVAL, S., TAKATS, Z., COOKS, R., and CAPRIOLI, R., "Mass spectrometric profiling of intact biological tissue by using desorption electrospray ionization," *Angew. Chem. Int. Ed*, vol. 44, pp. 7094–7097, 2005.

[97] WU, B., ABBOTT, T., FISHMAN, D., MCMURRAY, W., MOR, G., STONE, K., WARD, D., WILLIAMS, K., and ZHAO, H., "Comparison of statistical methods for classification of ovarian cancer using mass spectrometry data," *Bioinformatics*, vol. 19, no. 13, p. 1636, 2003.

[98] XU, C., PHAM, D. L., and PRINCE, J. L., "Finding the brain cortex using fuzzy segmentation, isosurfaces, and deformable surface models," in *IPMI* (DUNCAN, J. S. and GINDI, G., eds.), vol. 1230 of *Lecture Notes in Computer Science*, pp. 399–404, Springer, 1997.

[99] YEZZI, A. J., KICHENASSAMY, S., KUMAR, A., OLVER, P. J., and TANNENBAUM, A., "A geometric snake model for segmentation of medical imagery," *IEEE Trans. Med. Imaging*, vol. 16, no. 2, pp. 199–209, 1997.

[100] ZAI, G., KING, N., WIGG, K., COUTO, J., WONG, G., HONER, W., BARR, C., and KENNEDY, J., "Genetic study of the myelin oligodendrocyte glycoprotein (MOG) gene in schizophrenia," *Genes, Brain & Behavior*, vol. 4, no. 1, pp. 2–9, 2005.

[101] ZHANG, F., GOODLETT, C., HANCOCK, E. R., and GERIG, G., "Probabilistic fiber tracking using particle filtering," in *MICCAI (2)* (AYACHE, N., OURSELIN, S., and MAEDER, A. J., eds.), vol. 4792 of *Lecture Notes in Computer Science*, pp. 144–152, Springer, 2007.

[102] ZHU, L., HAKER, S., and TANNENBAUM, A., "Flattening Maps for the Visualization of Multibranched Vessels," *IEEE Transactions on Medical Imaging*, vol. 24, no. 2, pp. 191–198, 2005.

VITA

Vandana Mohan was born in Mumbai (then Bombay), India on September 3rd, 1982. She received her Bachelor's degree in Electronics and Communication Engineering from PSG College of Technology, Coimbatore, India in 2003 and worked with Oracle Corporation in India for over a year before coming to Georgia Tech to pursue her PhD. Her doctoral research focused on computer vision, specifically its application to the analysis and interpretation of medical imagery towards aiding clinicians and medical professionals in decision-making, both offline and as part of the surgical workflow. This work focused primarily on brain and cardiac disorders. During her PhD, she also explored the field of breast cancer detection via an internship with Siemens Medical Solutions where her work resulted in an invention disclosure on a novel pharmacokinetic model.